JOURNAL OF GEOPHYSICAL RESEARCH, VOL. 101, NO. C3, PAGES 6313–6335, MARCH 15, 1996

A study of the Kuroshio's seasonal variabilities using an altimetric-gravimetric geoid and TOPEX/POSEIDON altimeter data

Cheinway Hwang

Department of Civil Engineering, National Chiao Tung University, Hsinchu, Taiwan

Abstract. The first year of TOPEX/POSEIDON (T/P) altimeter data were used to study the seasonal variabilities of the Kuroshio Current. The intercomparison between the T/P and gauge sea levels at selected tide gauge stations around Taiwan shows that the two have a correlation of about 0.9 at the immediate vicinity of the deep ocean and both show an annual cycle with an amplitude of 15 cm. A $3' \times 3'$ geoid for the Western Pacific was constructed by least squares collocation using gravity anomalies and sea surface gradients derived from Seasat, Geosat, ERS 1, and T/P altimetry . To account for the oceanographic signal in the altimeter data, we derived a covariance function for the gradients of the sea surface topography (SST) based on a global averaging concept and a spherical harmonic expansion of the Levitus SST to degree 50. The accuracy of the geoid ranges from 5 to 40 cm. The SST values derived from the geoid and the data along T/P's descending tracks were fitted to the hyperbolic functions in a two-step procedure to find the Kuroshio's seasonal axes and the parameters that describe its characteristics. The mean variabilities in the Kuroshio's path, maximum velocity, baroclinic transport, and width are 22 km, 19 cm, 8 Sv, and 27 km, respectively. The averaged percentage variability of all quantities is 25%. All the variabilities are relatively large near the northeast coast of Taiwan and the starting point of the Kuroshio Extension. The large-scale circulations over the Western Pacific were obtained by median filtering the SST. At the 1334-km spatial scale, the Pacific's subtropical gyre is clearly visible, and it shows different features over the four seasons and its kinetic energy shows possible correlations with the determined parameters. Over the South China Sea a warm ring with a radius of 300-400 km and a center at 15°N, 113°E was detected in the spring and summer.

Introduction

In east Asia the Kuroshio Current, one of the western boundary currents, plays a key role on the local fishery, navigation, and circulation [*Tang and Yang*, 1993]. The Kuroshio is part of the circulation system of the Western Pacific Ocean. The Kuroshio begins at the east coast of Philippines; after leaving the northeast coast of Taiwan, it follows roughly the 200-m isobath before it reaches south of Japan [*Hu and Chang*, 1992]. In comparison to the Gulf Stream, which was extensively studied with satellite altimetry [e.g., *Tai*, 1990; *Zlotnicki*, 1991; *Rapp and Smith*, 1994], the Kuroshio did not receive the same attention with altimetry. (Note that researchers like *Tai* [1990] and *Zlotnicki* [1991] focused only on the Kuroshio Extension). The reason is unknown, but one could suspect that it is due to the lack of a good geoid or the lack of confidence in the altimeter data quality over this area, especially for data from Seasat and Geosat. In fact, the geoid plays a crucial role in extracting oceanographic signals over the western boundary currents such as the Gulf Stream and the Kuroshio [*Rapp and Smith*, 1994]. Over the Gulf Stream area several geoid models exist, e.g., the models of *Marsh and Chang* [1978], *Wessel and Watts* [1988], and *Porter et al.* [1992]. Recently, *Rapp and Wang* [1994] developed a geoid model for the Gulf Stream using marine gravity data and the model was used in a study of the Gulf Stream characteristics [*Rapp and Smith*, 1994]. However, little attention is paid to the construction of a detailed geoid over the Kuroshio, although such works do exist, e.g., Fukuda's altimetric-gravimetric geoid cited by Segawa [1991, p. 128]. In fact, the Kuroshio travels through a much more complex gravity field than the Gulf Stream area, so the need of a high-resolution geoid for the Kuroshio is more critical than the Gulf Stream. Thus, in this study, one of the primary goals is to construct a detailed local geoid using existing altimeter data and gravity data. Altimeter

Copyright 1996 by the American Geophysical Union.

Paper number 95JC03800.
0148-0227/96/95JC-03800$05.00

data will be used because with the sparse gravity data alone (see below), there will be no possibility of getting a high-resolution geoid. However, altimeter data contain gravity signals as well as the oceanographic signals, which must be carefully taken into account when computing the geoid. Such an altimetric-gravimetric geoid should fulfill the requirements that it can not only be used for determining the short wavelength signals such as the fronts of the Kuroshio but also for identifying the long wavelength features such as the general circulation of the Western Pacific. With a precision geoid, the next goal of this study is then to quantify the seasonal variabilities of the Kuroshio from the TOPEX/POSEIDON (T/P) data.

In the context of this study the Western Pacific is defined to be within 105°E - 140°E and 5°N - 35°N and the Kuroshio Extension will not be covered. It is known that the primary goal of the T/P mission has been to determine the general circulation of the oceans [*Fu et al.*, 1994]. For a study of this kind a global data set is prepared, and normally the data over shallow seas are excluded. One of the reasons for data exclusion over shallow seas is due to the uncertainty in the ocean tide model. On the other hand, *Mazzega and Bergé* [1994] have computed the major tidal components in the Asia semiclosed Seas [such as the South China Sea and the Japan Sea] and obtained promising results, implying that the T/P altimeter system (including the orbit, geophysical corrections, and other factors affecting the measured sea surface height) over shallow seas should function very well except for the tide models. Furthermore, when doing intercomparison between the T/P sea level and tide gauge sea level, researchers tend to select the gauge stations in the deep ocean, and it has not been shown whether the comparison over shallow seas will yield the same good agreement as for the deep ocean. For scientists who pay more attention to a local area than the entire globe these are the questions they often raise and they are keen to know the answers, especially when the studied area has a possibly unfavorable condition for the T/P altimeter system. Thus we will first investigate the performance of the T/P altimeter system over the studied area using tide gauge measurements. We will focus on both the numerical technique of geoid computation and the analysis of the sea surface topography (SST) regarding the characteristics of the Kuroshio and the Western Pacific.

TOPEX/POSEIDON Data Processing and Averaging

The T/P data used in this study were supplied by *Archiving, Validation, and Interpretation of Satellite Data in Oceanography (AVISO)* [1992]. It is the sea surface height (SSH) above the reference ellipsoid that will be used in our analyses. In order to obtain reliable SSH , the criteria used by *Denker* [1990] were employed to edit the Geophysical Data Records (GDRs). After passing the editing criteria, geophysical corrections were applied to the instantaneous SSHs. In other altimeter missions such as Seasat and Geosat, the accuracy of satellite orbit has been a primary error source for SSH . However, the 5-cm radial orbit accuracy of T/P [*Tapley et al.*, 1994a] is now comparable to the errors of geophysical corrections. In particular, we expect the error in ocean tide model at the vicinity of continental shelf or shallow seas will probably exceed the T/P orbit error. For a geophysical correction the T/P GDRs contain various models for use. Figure 1 compares the various models of ionospheric correction, wet tropospheric correction, and ocean tide along arcs a025 and d081 of cycle 18. These two arcs, whose ground tracks are plotted in Figure 2, travel from the deep ocean to shallow seas and from the tropic to the high latitude. Arcs a025 and d081 correspond to passes 51 and 164 defined by *AVISO* [1992]. The symbol "a" stands for "ascending," and "d" is for "descending." This convention will also be used in other figures of this paper. The formula for conversion between arc and pass is pass = 2 arc+1 for an ascending arc, and pass = 2 (arc + 1) for a descending arc. We notice from Figure 1 that south of 20°N the difference in ionospheric correction between the T/P model and Doppler orbitography and radio positioning integrated by satellite (DORIS) model is about 5 cm, which is the size of the T/P radial orbit error. Since the T/P ionospheric model is direct from the dual-frequency measurements and has accuracy of the order of 1 cm [*Imel*, 1994], it is selected for correcting the TOPEX range measurements; for the POSEIDON measurements, the DORIS ionospheric model is adopted because the result from *Escudier et al.* [1993] has shown that it provides sufficient accuracy for a single-frequency altimeter. The root mean squared (rms) difference of the two wet tropospheric models is also about 5 cm, and the difference is particularly large in the tropical area. The radiometer model was adopted for the wet tropospheric correction. As far as the ocean tides are concerned, the Cartwright and Ray model and the modified enhanced Schwiderski agree quite well in the open ocean, but the two have large differences over shallow seas, reaching 30 cm. Many studies, e.g., *Eanes et al.* [1993], have confirmed that the Cartwright and Ray model has a better accuracy than the modified enhanced Schwiderski; thus the former was used in this study. Recent works by, e.g., *Ma et al.* [1994], *Schrama and Ray* [1994], and *Knudsen* [1994], have improved the Cartwright and Ray model by 1-2 cm, and we expect that the application of these new tide models to the T/P GDR will improve our analysis. A note is given to the correction due to different flattenings of the reference ellipsoids used by TOPEX and POSEIDON. The correction is [*Rapp*, 1989]

$$\Delta h = \frac{a\Delta f(1-f)\sin^2\phi}{W} \qquad (1)$$

where Δf=1/298.257 - 1/298.25653577, $W = \sqrt{1-(2f-f^2\sin^2\phi)}$, and a, f, ϕ are the equatorial radius (6378136.3 m), flattening, and latitude, respectively. Here Δh increases from zero at the equator to -2.8 cm at latitude= ±66° and is to be added to a PO-

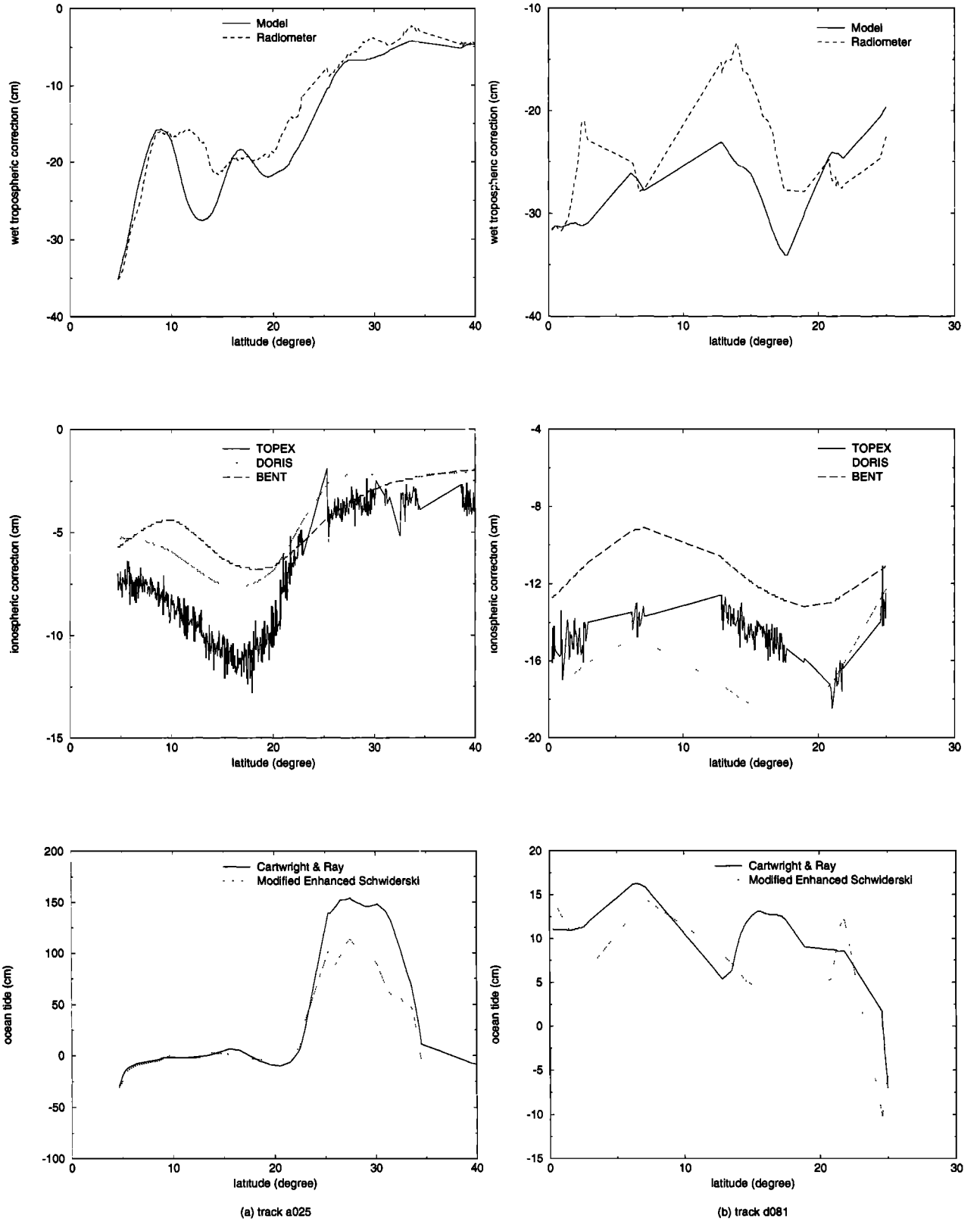

Figure 1. Comparison of various models of geophysical corrections in the TOPEX/POSEIDON Geophysical Data Records for track d081 and track a025. For the ionospheric corrections, the DORIS and Bent models are defined in AVISO (1992).

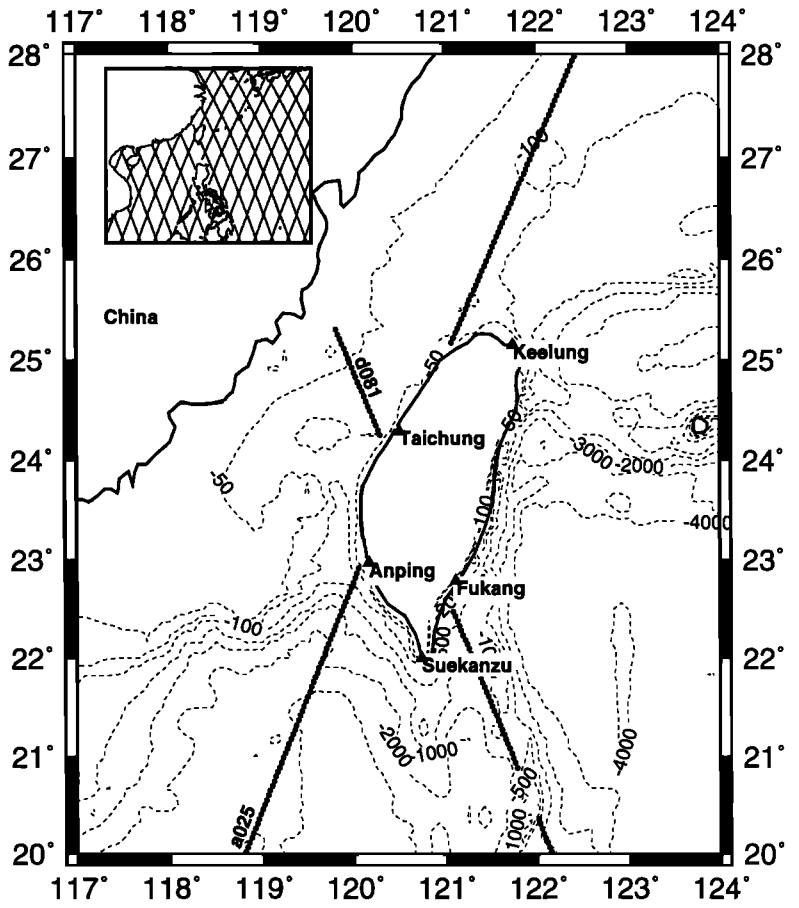

Figure 2. Distribution of selected tide gauge stations for T/P sea level comparison; also shown are T/P tracks a025 and d081. The contours (dashed lines) are bathymetry at selected depths. The inserted map shows all the T/P ground tracks over 105°E - 140°E and 5°N - 35°N.

SEIDON's SSH in order to make the two height systems consistent.

For later development the SSH from the first 36 cycles are averaged according to seasons, and a final averaging is made for one year. The relationship among the first 36 repeat cycles, dates, and the four seasons is given in Table 1. Because of the highly accurate orbit, the T/P SSH were not subject to orbit adjustment, which is the common practice for data from other satellite missions. Also, the adjustment of the T/P orbit may have the possibility of removing oceanographic signals. Note that *Tai and Kuhn* [1994] have adjusted the T/P altimeter data and obtained improved orbits. The averaging cannot remove the geographically correlated orbit error (if any) and nonperiodic time-varying errors introduced by the geophysical corrections. The averaging certainly can reduce the random errors due to the altimeter itself and the instruments for obtaining geophysical correction models. The averaging can also reduce the periodic time-varying errors if the period of averaging happens to coincide with or is close to the integral multiple of the period of the error. For example, all the major ocean tide components have periods less than 1 month, and the 3-month averaging period for a season should reduce the major tidal errors.

Table 1. Relationship Among the First 36 Repeat Cycles, the Dates, and the Four Seasons

Cycles	Dates	Season
1-9	Sept. 22, 1992 to Dec. 21, 1993	fall
10-18	Dec. 22, 1993 to March 21, 1993	winter
19-27	March 22, 1993 to June 21, 1993	spring
28-36	June 22, 1993 to Sept. 21, 1993	summer

Verification of the TOPEX/POSEIDON System Using Tide Gauge Data

To evaluate the T/P altimeter system over the Kuroshio, we compare the monthly sea level as measured by T/P and by tide gauges at five selected tide gauge stations around Taiwan (Figure 2). The stations Keelung and Fukang are at the immediate vicinity of the deep ocean, and the rest lie on the shallow seas west of Taiwan. Note that the mean sea level at Keelung is the vertical datum of Taiwan. Since we are interested in the seasonal variation of of the sea level, the gauge data were averaged monthly to remove the ocean tide effect. To obtain the monthly T/P sea levels, for each repeat cycle we first construct a 1° × 1° grid from the along-

Table 2. Correlation Coefficients Between TOPEX/POSEIDON and Gauge Sea Levels

Gauge Station	Coefficients
Keelung	0.828
Taichung	0.541
Anping	0.482
Suekanzu	0.734
Fukang	0.909

track SSH using a minimum curvature fitting [*Wessel and Smith*, 1991] for an area covering all the stations. Three such grids from three consecutive cycles are averaged to yield a monthly grid. The sea level at a desired tide gauge station is then obtained by interpolation. This method does not work well for the station Fukang, so for this particular station we decided to get the monthly sea level by averaging all the SSH within 100 km of the station. Table 2 shows the correlation coefficients between the T/P and gauge sea levels. From Table 2 we see that the two sea levels which are at the boundary of the deep ocean have a high correlation at the east coast of Taiwan. Over shallow seas the performance of the T/P altimeter system is only fair as indicated by the low correlation coefficients there, which are probably due to tide model errors. Figure 3 shows the monthly sea levels from T/P and tide gauges at Keelung and Fukang, where the correlation coefficients are 0.828 and 0.909, respectively. Both the T/P and the gauge sea levels appear as a cosine function with a 1-year period. The zero phase (or the highest sea level) occurs in August, and the amplitude is about 15 cm. According to *Tang and Yang* [1993], the rise and fall of the sea level at Keelung are strongly correlated with the activity of the Kuroshio. As the Kuroshio "intrudes" into the continental shelf of the East China Sea in around mid-October, the sea water was carried away by the Kuroshio from the shore of the northern Taiwan, causing the sea level at Keelung to descend. The "intrusion," as well as the decrease of the sea level at Keelung, continues all the way to March. From March, the Kuroshio gains its strength gradually by perhaps the heating in the tropic, and it begins to move toward the deep ocean (i.e., to the east). The accompanying rise of the sea level at Keelung beginning in March is due to in part the cease of the "intrusion" and in part the overall increase of the water mass carried by the Kuroshio. The implication of this comparison is that the T/P altimeter system may perform very well even at the vicinity of the deep ocean.

An Altimetric-Gravimetric Geoid Over the Western Pacific

The Method

The method we will use to construct a local geoid for the Western Pacific is least squares collocation (LSC) [*Moritz*, 1980], which is the only known geodetic technique in using heterogeneous data. First, we will discuss the altimeter data type to be used. The altimeter-measured sea surface heights contain both geodetic and oceanographic signals and measuring errors. Except for T/P, the data errors have largely come from the satellite's orbit. Considering all these effects, an altimetric SSH, not including the random noise, may be expressed as

$$h = \zeta + N + b \tag{2}$$

where ζ is the SST, N is the geoidal height, and b is the orbit error, which is assumed to be a constant within a arc of less than, say, 4000 km. To avoid the error b, we may use the along-track sea surface gradient (SSG) obtained by

$$e(\alpha) = \frac{\partial h}{\partial s} = \frac{\partial \zeta}{\partial s} + \frac{\partial N}{\partial s} = \theta(\alpha) + \epsilon(\alpha) \tag{3}$$

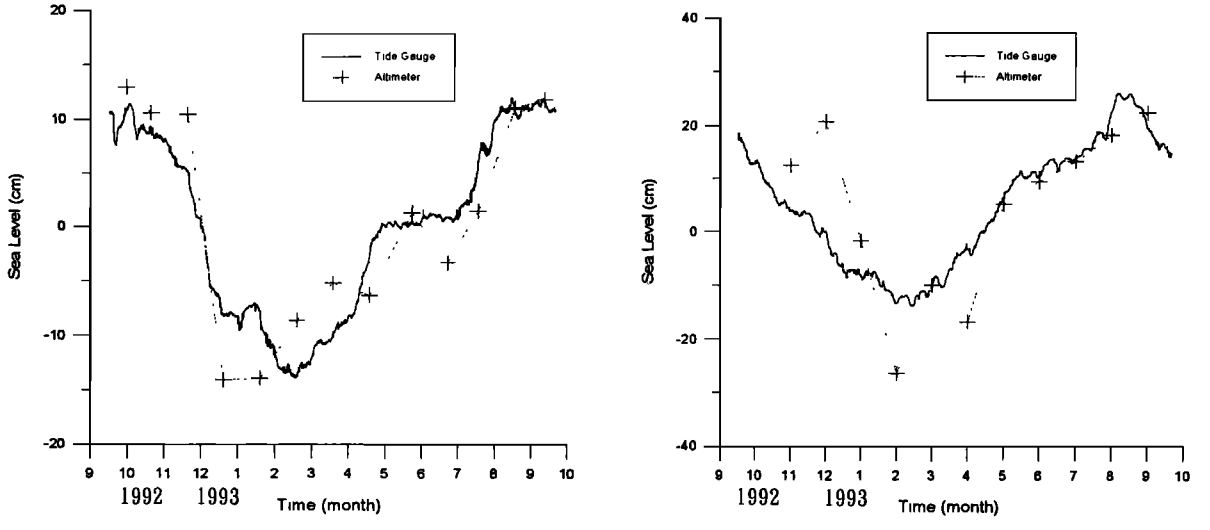

Figure 3. Comparison of sea levels measured by tide gauges and by T/P altimeter at (left) Fukang and (right) Keelung. For both sea levels the mean values from their respective yearly averages are removed.

where α is the azimuth of the track which may be calculated by an approximate formula by *Hwang and Parsons* [1995]. Note that the azimuth varies along the track. Thus a SSG contains both the SST gradient and the geoid gradient which is a functional of the Earth's gravity field. Another type of data related to the geoid is gravity anomaly. With SSG and gravity anomalies as data, we can use LSC to predict geoidal heights. To this end we will have to determine the required covariance functions. Assuming the geoid gradient and SST gradient are uncorrelated, the covariance function of SSG is the sum of the covariance functions of geoid and SST gradients:

$$C_{ee} = C_\theta + C_\epsilon \tag{4}$$

The covariance function of geoid gradient, C_ϵ, has been derived by *Hwang and Parsons* [1995] (Appendix A). The covariance function of SST gradient C_θ may be derived using the procedure of *Moritz* [1972] and *Moritz* [1980]. First, we expand the SST into a series of spherical harmonic functions as

$$\zeta(\phi,\lambda) = \sum_{n=0}^{K}\sum_{m=0}^{n}\left(\bar{a}_{nm}\cos m\lambda + \bar{b}_{nm}\sin m\lambda\right)\cdot \bar{P}_{nm}(\sin\phi) \tag{5}$$

where ϕ and λ are latitude and longitude, $\bar{P}_{nm}$ is the fully normalized associated Legendre function of degree n and order m, and K is the maximum expansion degree. Using the analogy in deriving the covariance function of the Earth's disturbing potential, the global covariance function of SST is

$$\begin{aligned} C_\zeta(\psi) &= M\left[\zeta(\phi,\lambda)\zeta(\phi',\lambda')\right] \\ &= \frac{1}{8\pi^2}\int_{\lambda=0}^{2\pi}\int_{\phi=-\pi/2}^{\pi/2}\int_{\alpha=0}^{2\pi}\zeta(\phi,\lambda)\zeta(\phi',\lambda')\cdot \cos\phi\, d\phi\, d\lambda\, d\alpha \\ &= \sum_{n=0}^{K}\zeta_n P_n(\cos\psi) \end{aligned} \tag{6}$$

where M is the global averaging operator, ψ is the spherical distance, P_n is the Legendre polynomial, and ζ_n is the degree variance of the SST defined as

$$\zeta_n = \sum_{m=0}^{n}\left(\bar{a}_{nm}^2 + \bar{b}_{nm}^2\right) \tag{7}$$

With the covariance function of SST we can then determine the covariance function of SST gradient using the law of covariance propagation [*Moritz*, 1980]. First, we have to determine the isotropic covariance functions of SST gradient. Using the method of *Moritz* [1972] and *Tscherning and Rapp* [1974], the covariance functions of the longitudinal and transverse components of SST gradient, which are isotropic, are

$$C_{ll}^{\zeta} = (tC_\zeta' - \sin^2\psi C_\zeta'')/R^2 \tag{8}$$

$$C_{mm}^{\zeta} = C_\zeta'/R^2 \tag{9}$$

where $t = \cos\psi$ and R = 6371 km is the Earth's mean radius. Using (6) we have

$$\begin{aligned} C_\zeta'(t) &= \frac{d}{dt}[C_\zeta(t)] = \sum_{n=0}^{K}\zeta_n P_n'(t) \\ &= \sum_{n=0}^{K} n\zeta_n\left[\frac{1}{1-t^2}P_{n-1}(t) - \frac{t}{1-t^2}P_n(t)\right] \end{aligned} \tag{10}$$

and

$$\begin{aligned} C_\zeta''(t) &= \frac{d^2}{dt^2}[C_\zeta(t)] = \sum_{n=0}^{K}\zeta_n P_n''(t) \\ &= \sum_{n=0}^{K} n\zeta_n\left[\frac{2t}{(1-t^2)^2}P_{n-1}(t) - \frac{(1-n)t^2+n+1}{(1-t^2)^2}P_n(t)\right] \end{aligned} \tag{11}$$

In the above two equations the differential relationships of Legendre's polynomial [*Lebedev*, 1972] have been employed. Note that when $t = \pm 1$, singularities will occur and they are treated in Appendix A. Following the procedure of *Hwang and Parsons* [1995] for deriving the covariance function of geoid gradient, the covariance function between a SST gradient at P with azimuth α_P and a SST gradient at Q with azimuth α_Q is

$$\begin{aligned} C_\theta(P,Q) = {} & C_{ll}^{\zeta}\cos(\alpha_P - \alpha_{PQ})\cos(\alpha_Q - \alpha_{PQ}) + \\ & C_{mm}^{\zeta}\sin(\alpha_P - \alpha_{PQ})\sin(\alpha_Q - \alpha_{PQ}) \end{aligned} \tag{12}$$

where α_{PQ} is the azimuth from P to Q. Furthermore, the covariance of geoid gradient has exactly the same form as $C_\theta(P,Q)$ [*Hwang and Parsons*, 1995]:

$$\begin{aligned} C_\epsilon(P,Q) = {} & C_{ll}^{\epsilon}\cos(\alpha_P - \alpha_{PQ})\cos(\alpha_Q - \alpha_{PQ}) + \\ & C_{mm}^{\epsilon}\sin(\alpha_P - \alpha_{PQ})\sin(\alpha_Q - \alpha_{PQ}) \end{aligned} \tag{13}$$

where C_{ll}^{ϵ} and C_{mm}^{ϵ} are the covariance functions of the longitudinal and transverse components of geoid gradient. Thus the covariance function of SSG is

$$\begin{aligned} C_{ee} = {} & (C_{ll}^{\zeta} + C_{ll}^{\epsilon})\cos(\alpha_P - \alpha_{PQ})\cos(\alpha_Q - \alpha_{PQ}) + \\ & (C_{mm}^{\zeta} + C_{mm}^{\epsilon})\sin(\alpha_P - \alpha_{PQ})\sin(\alpha_Q - \alpha_{PQ}) \end{aligned} \tag{14}$$

Other required covariance functions are those for geoid-SSG, gravity anomaly-SSG, geoid-gravity anomaly, and gravity anomaly-gravity anomaly. Assuming zero correlation between the Earth's gravity field and and the SST, the covariance function for geoid-SSG is

$$\mathrm{cov(N,e)} = \mathrm{cov(N,}\epsilon\mathrm{)} = \mathrm{C_{N\epsilon}} = -\cos(\alpha_Q - \alpha_{PQ})\mathrm{C_{lN}} \tag{15}$$

and the covariance function for gravity anomaly-SSG is

$$\mathrm{cov}(\Delta g,\mathrm{e}) = \mathrm{cov}(\Delta g,\epsilon) = \mathrm{C_{\Delta g\epsilon}} = -\cos(\alpha_Q - \alpha_{PQ})\mathrm{C_{l\Delta g}} \tag{16}$$

where C_{lN} and $C_{l\Delta g}$ are the covariance functions between the longitudinal component of geoid gradient and

geoidal height and gravity anomaly, respectively. Equation (15) and (16) are again based on the derivations by *Hwang and Parsons* [1995]. In this study, except C_{ll}^{ζ} and C_{mm}^{ζ}, all other required isotropic covariance functions were constructed with the Model 4 degree variance of *Tscherning and Rapp* [1974].

The degree variances in (7) were determined using a spherical harmonic expansion of the Levitus SST [*Levitus*, 1982]. The maximum expansion degree K is 50, which is high enough to recover most of the spectra of the Levitus SST; see also the discussion by *Engelis* [1987]. In the spherical harmonic expansion, the SST land values are assumed to be zero. Figure 4 shows the two isotropic covariance functions of SST gradient, which have low variances and large correlation lengths due to the long wavelength nature of the Levitus SST.

In the practical use of LSC, we employed the so-called remove/restore procedure with the Ohio State University 1991 gravity model (OSU91A) to degree 360 [*Rapp et al.*, 1991] as the reference field. The error parts of the covariance functions are computed using the error estimates of OSU91A coefficients in a Legendre polynomial series [*Hwang and Parsons*, 1995]. A LSC computation is carried out in a $0.25° \times 0.25°$ inversion cell with a data border of 0.60° which is selected based on numerous tests. This choice of cell size and data border requires least computational time, and the large ratio between the data border and the cell size has ensured a smooth transition of the predicted geoidal heights between two adjacent cells. Furthermore, because the LSC computations are made locally, all the covariance functions mentioned above must be scaled to reflect the local behaviors of the covariance functions. For the prediction formulae, use of covariance functions in the remove/restore procedure, and use of scaling factors, see Appendix B and the work of *Hwang and Parsons* [1995].

The Data and the Result

Using the method of LSC, we have computed a $3' \times 3'$ geoid over the Western Pacific on a CONVEX-3840 supercomputer. Due to the enormous amount of data, a total of 29 CPU hours is consumed. The SSG used are from Seasat, Geosat/Exact Repeat Mission (ERM), ERS 1 35-day, ERS 1/Geodetic Mision (GM), and T/P data. At latitude = 26°, the typical data density is 300 points in a $1° \times 1°$ cell. The ERS 1/GM includes data from the first 168 days of the geodetic mission and has a very dense data distribution. However, the accuracy of ERS 1/GM is the poorest among all data. The ERS 1 35-day data are based on 18 cycles average, and the T/P data are based on the first 36 cycles average. All these gradients have different qualities, and their error variances form the diagonal elements of D_e in (B5). The error variances of the SSG are obtained by the simple statistics that use the repeat measurements on the same location. It is clear that an "error variance" computed in such a manner contains both the white noise spectrum and the variability of the sea surface. Thus the error variances may not have the desired normal distribution. However, a SSH with a high variability,

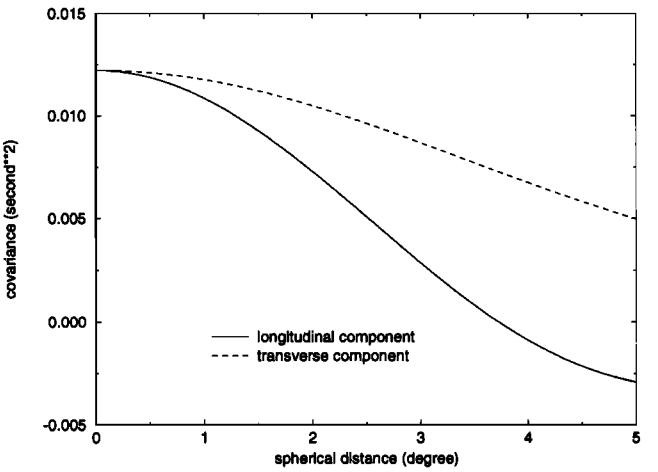

Figure 4. Covariance functions of the longitudinal and transverse components of sea surface topography (SST) gradient. Both have relatively long correlation lengths, due to the long wavelength nature of the SST.

and hence a large error variance, will yield a less reliable mean SSH over a limited time span of averaging. Therefore an observation with a large error variance will be less weighted, and this is precisely what we want in the LSC computations. Seasat and ERS 1/GM do not have repeat measurements so we assign a uniform standard deviation of 10 μrads for them, based on the estimated 5-cm noise of range measurement and 6.73-km along-track distance [*Hwang and Parsons*, 1995].

The gravity anomalies used contain data both on land and on sea. Figure 5 shows the data distribution. In fact, for the land values, only data over Taiwan, which are collected by *Yen et al.* [1990] in a 7-year campaign, are used. The marine gravity anomalies are from the National Geophysical Data Center (NGDC) database, and the data density is low along the path of the Kuroshio. The sparsity justifies the need of high-density altimeter data. The quality of marine gravity varies from one cruise to another, but its white noise is believed to be well below 1 mgal [*Hwang and Parsons*, 1995]. For the LSC computations it is decided to assign an uniform standard deviation of 1 mgal for all the gravity data. The land gravity anomalies over Taiwan are important for the determination of the Kuroshio's variability east of Taiwan. This is because near coastal areas, altimeter data are edited out; the use of land data will help to increase the resolution and accuracy of the predicted geoid there. Furthermore, terrain corrections for the land gravity anomalies, computed using the fast Fourier transform technique described by *Schwarz et al.* [1990], are applied using a $30'' \times 30''$ digital terrain model. Due to the rugged terrain over Taiwan, the maximum terrain correction is 70 mgals with a mean and a standard deviation of 2.2 and 5.3 mgals, respectively. As given by *Hwang and Parsons* [1995], the marine gravity anomalies are adjusted by a quadratic polynomial with respect to the satellite gravity anomalies derived from Seasat, Geosat/ERM, ERS 1 35-day, and T/P data.

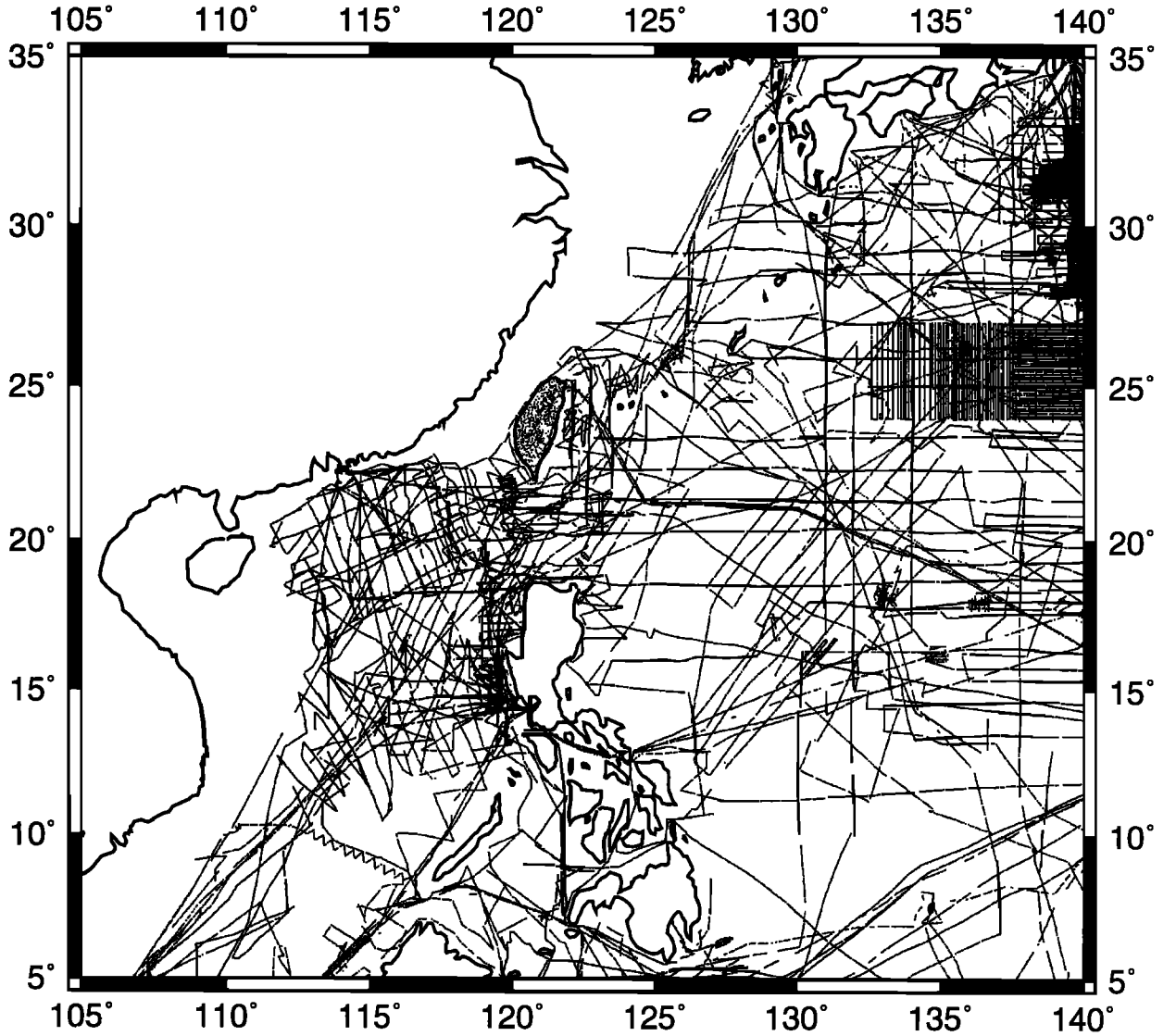

Figure 5. Distribution of marine and land gravity anomalies. For land values, only data over Taiwan are available.

Figure 6 shows the predicted marine geoid over the Western Pacific. This local geoid clearly reveals the high-frequency tectonic structures, e.g., the Philippine Trench, the Ryukyu Trench, and the Ryukyu Islands. Since the Kuroshio travels through the Philippine Trench, the east coast of Taiwan, and the boundary of the Ryukyu Islands, one would need such a high-resolution geoid to identify its fronts as its width could be well below 100 km; see also the development below. Figure 7 shows the error estimates of this local geoid. From Figure 5 to Figure 7, two points may be concluded: (1) the use of marine gravity anomalies will reduce the geoid error, and, in general, the geoid error is below 5 cm in the presence of highly dense gravity anomalies, e.g., the spots near 25°N, 140°E, and 20°N, 115°E; and (2) in the areas of high-frequency geoid variation, e.g., the trench areas and islands, the error is large. Special attention must be given to the geoid error along the Kuroshio's path. From Figure 7, the geoid error along its path varies from the minimum of 15 cm near the 200-m isobath to the maximum of 35 cm near the east coast of Taiwan. The fact that the predicted geoid is subject to errors indicates that the true resolution may not be $3' \times 3'$ and the predicted geoid should be filtered in some way before use. We finally note that the error of the predicted geoid is much less than the 49-cm commission error of the geoid from OSU91A to degree 360 [*Rapp*, 1993].

Seasonal Variability of the Kuroshio

By subtracting the altimetric-gravimetric geoid from the averaged T/P SSH , one gets the SST for further uses. One of the uses is to study the seasonal variability of the Kuroshio. First, we will investigate the "shape" of the SST across the Kuroshio front and determine the parameters of interest (see Figure 6.23 and Table 6-1 of *Apel* [1987] for the definition of the "front" of a western

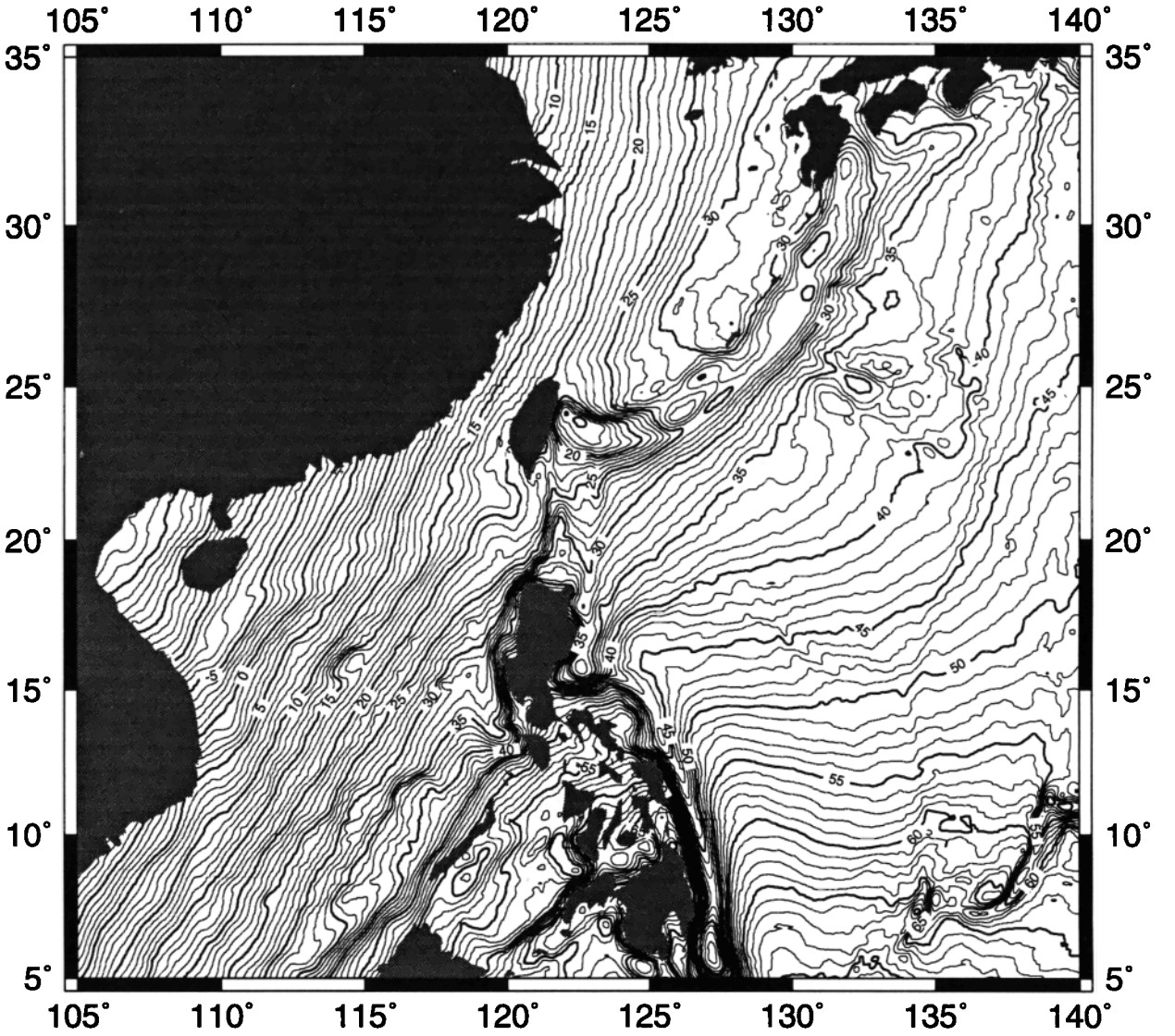

Figure 6. The predicted altimetric-gravimetric geoid over the Western Pacific; contour interval is 1 m.

boundary current). Following the works by *Zlotnicki* [1991] and *Rapp and Smith* [1994], the along-track SST across the Kuroshio front can be approximated by the hyperbolic function:

$$\zeta(x) = H\tanh(\frac{x - x_0}{L}) + \zeta_0 \qquad (17)$$

where the parameters to be determined are [*Rapp and Smith*, 1994] H, $2H$ is the height jump, which will be denoted as $\Delta\eta$ below; x_0, which corresponds to the location where the maximum geostrophic velocity occurs (see below); L, $1.89L$ is the along-track width of the Kuroshio; and ζ_0, an unknown constant.

Note that one can also use the error function for approximating the SST, as given by *Tai* [1990] and *Rapp and Smith* [1994]. The along-track width of $1.89L$ is based on the 45.6 % falloff of the velocity at the edge of the Kuroshio [*Rapp and Smith*, 1994, p. 24,709]. The along-track distance x increases in the satellite's flight direction. By this definition a positive velocity will be to the left when viewing toward the positive x direction. The height jump may be used to estimate the baroclinic transport with a two layer approximation as suggested by *Tai* [1990]; see also *Zlotnicki* [1993]. By that approximation, for a mean thermocline depth of 500 m the relationship between height jump ($\Delta\eta$) and baroclinic transport at midlatitudes is

$$\text{baroclinic transport} = 50\Delta\eta \qquad (18)$$

where the unit for baroclinic transport is 10^6 m^3 s^{-1} (Sv) and the unit for $\Delta\eta$ is meters. Thus by (18), 1-m height jump corresponds to 50-Sv baroclinic transport.

The problem of determining the four parameters is nonlinear, and we use the following procedure to find the solution:

1. Determine the maximum geostrophic velocity and x_0. With the geostrophic equation the velocity field corresponding to the SST function in (17) is

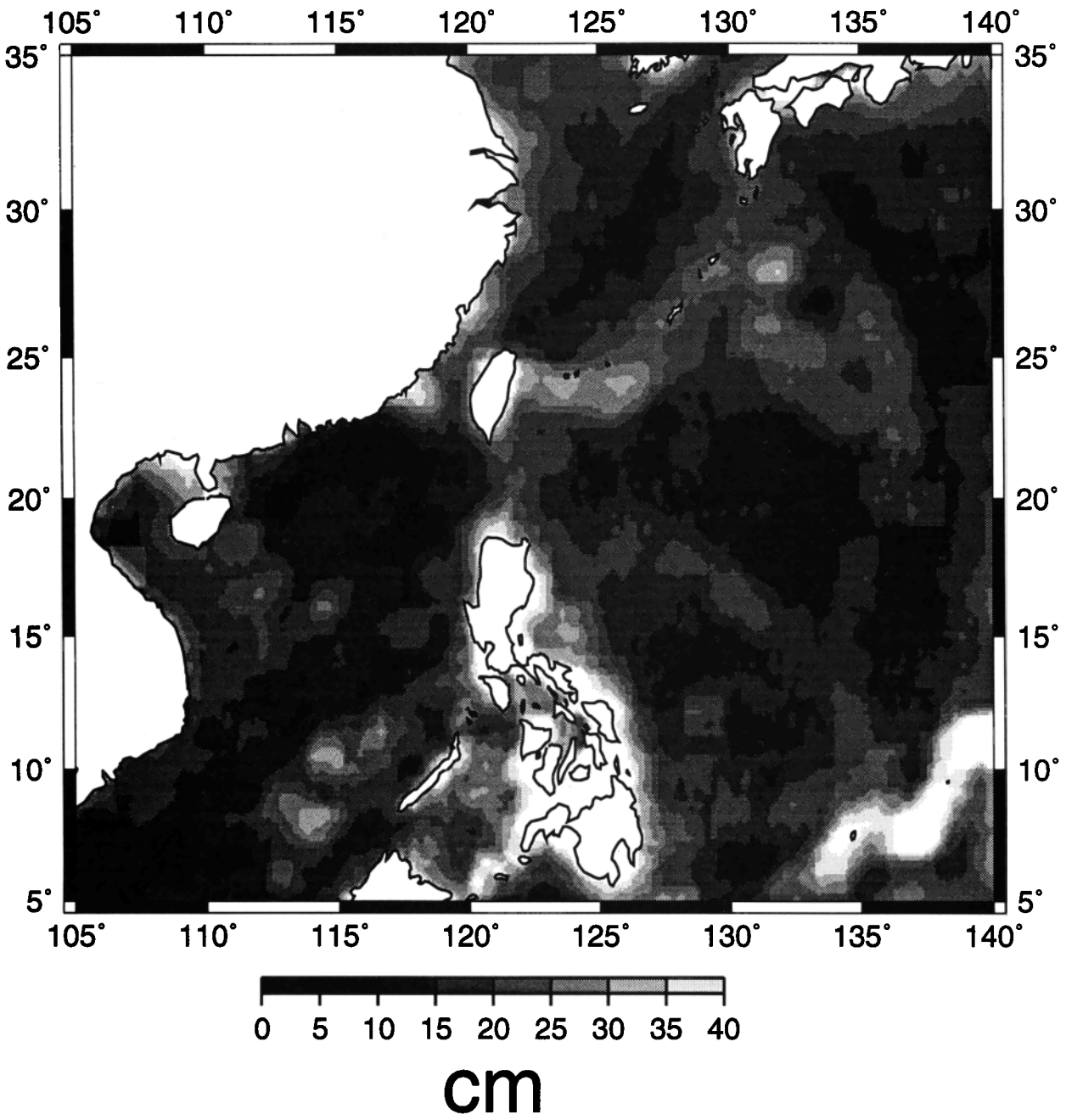

Figure 7. A gray-shaded map of the error estimates of the altimetric-gravimetric geoid (see Figure 6). Errors over land or larger than 40 cm are masked with white.

$$v(x) = \frac{g}{f}\frac{\partial \zeta}{\partial x} = \frac{gH}{fL}\mathrm{sech}^2\left(\frac{x - x_0}{L}\right) \tag{19}$$

where g is the normal gravity and $f = 2\Omega \sin\phi$ with Ω being the Earth's rotational velocity ($7.292115 \times 10^{-5}\mathrm{rads}^{-1}$). The maximum velocity occurs at $x = x_0$ and is

$$v_{max} = \frac{gH}{fL} \tag{20}$$

Therefore we first smooth the SST data using a filter, and then use numerical differentiation to find $\partial\zeta/\partial x$ and $v(x)$. Among all the velocity values, there exists a maximum which is the desired v_{max} and the corresponding x is x_0. From x_0 we then calculate the location of v_{max}, which can be viewed as the axis of the Kuroshio. Once v_{max} is found, (20) becomes a condition which the parameters H and L must satisfy, so now we are left with only two parameters to estimate: H (or L) and ζ_0.

2. Find H and ζ_0 by linearization and iterations. For the remaining parameters H and ζ_0 we may form the observation equation for a filtered SST value as

$$\zeta + v_\zeta = H\tanh\left[\frac{fv_{max}(x - x_0)}{gH}\right] + \zeta_0 \tag{21}$$

where v_ζ is the residual of the SST value ζ. The nonlin-

ear model of (21) can be linearized, and H and ζ_0 are solved by the least squares method with iterations; see, e.g., *Uotila* [1986].

With the above two-step procedure, we have estimated the four parameters along each of the T/P descending tracks over the area north of 20°N. The ascending tracks were not used because of their unfavorable geometry with respect to the Kuroshio's path. The Gaussian filter with a width of 50 km was used in order to find v_{max} (the filter width is the value d in equation (5) of *Tai* [1990]). About 5-10 iterations are required with a convergence criterion of 0.01 cm. During the estimation we assume all the T/P SST have a standard deviation of 15 cm, based on the geoid error and T/P's noise level. Thus we also have error estimates for H which then yields the error estimate for L. The error estimates of H and L can then be used to compute the error estimates of height jump and width by error propagation. Note that this error estimate indicates only the goodness of fit between the observed SST values and the hyperbolic model. An external check of the accuracies of the parameters will rely on the in situ data which are hard to collect on this time and spatial scale. The estimations have been carried out for the first four seasons and for the first year of the T/P mission. The estimated maximum velocities, height jumps, and along-track width are listed in Table 3. These parameters fluctuate over seasons, and, in general, high values occur in the spring and summer and low values occur in the fall and winter. Because we are only estimating two parameters instead of four in the least squares, the correlations between the estimated parameters are generally low (most below 20%). The high and low correlations are reflected as the large and small standard deviations of the estimated parameters in Table 3. As we examined the goodness of fit for all the tracks by visual comparison, we found that the hyperbolic model seems to work very well for the Kuroshio area. Figure 8 shows two typical comparisons, using tracks d119 and d017. Also, for all the tracks we found that the best data extent for model fitting is within 100 km to the axis.

Figure 9 shows the filtered along-track SST values and the locations where v_{max} were found. As stated before, the locations of v_{max} correspond to the axis of the Kuroshio. Figure 10 shows the locations of v_{max} and the filtered SST from the 1-year data. In Figure 10 we also make a comparison of the SST by using two different geoid models as the level surface: the altimetric-gravimetric geoid and the geoid from OSU91A to degree 360. The OSU91A geoid has a resolution of 50 km and certainly cannot fully account for the complex bottom topography along the path of the Kuroshio. Because of its relatively low resolution, with the OSU91A geoid, one cannot tell whether the steep slope in the computed SST is due to the gravity signal or oceanographic signals such as the Kuroshio front, and this is why in Figure 10 (lower panel) we cannot identify the location of the Kuroshio with the OSU91A geoid. Furthermore, we treated the locations of the path as a function of the along-path distance, namely

$$\phi = \phi(s), \qquad \lambda = \lambda(s) \tag{22}$$

where s is the along-path distance. Then we fitted a spline to the observed locations to obtain the path of the Kuroshio. Note that Akima's spline [*de Boor*, 1978] was used to avoid large oscillations due to the unequally spaced knots. Figure 11 shows the computed paths for the four seasons and for one year with the altimetric-gravimetric geoid as the level surface. Also, the path from the 32-year averaged Geomagnetic Electro-Kinetograph (GEK) data is compared with the path from the 1-year T/P data in Figure 11. GEK measures the velocity of currents utilizing the change of geomagnetic field caused by the flow of water; see *Pickard and Emery* [1982] for more details about the principle of GEK. The GEK path is obtained by digitizing Figure 2 of *Qiu et al.* [1990]. In general, the GEK path and the 1-year altimeter path agree very well. The GEK path follows the 200-m isobath after leaving Taiwan, whereas the altimeter path shifts about 0-50 km to the west of this isobath. The highly focused paths in all seasons at about 32°N, 132°E are in good agreement with the observations by *Mizuno and White* [1983]. Due to the large cross-track spacing of the T/P, the resolution of the altimeter path is limited; for example, the altimeter path cannot account for the sharp turn of the Kuroshio at about 30°N, 129°E.

To quantify the seasonal variability of the Kuroshio, we again use the estimated parameters in Table 3. For each of the tracks we calculate the standard deviations of the parameters based on the four values in the four seasons. The standard deviations may be treated as the variabilities. It is found that the mean variabilities in path, maximum velocity, height jump, and width are 22 km, 15 cm s^{-1}, 19 cm, and 27 km, respectively. The 19-cm height jump corresponds to 9.5-Sv baroclinic transport. If one accepts the idea that the percentage variability is the ratio between the standard deviation and the mean value, it is found that the average percentage variabilities in maximum velocity, height jump, and width are 19%, 28%, and 24%, respectively. Figure 12 shows the along-path variabilities for the axis, maximum velocity, height jump, and width. One sees from Figure 12 that all the variabilities are relatively large near the northeast coast of Taiwan and the beginning point of the Kuroshio Extension (at about 33°N, 137°E). A spot near 28°N, 128°E where the Kuroshio is about to make a sharp turn to the east also shows large variabilities in height jump, and width. Over the south coast of Japan the path variability is small, but the variabilities in maximum velocity, height jump, and width are large. Numerous studies have been devoted to the seasonal variability of the Kuroshio northeast of Taiwan [e.g., *Chern et al.*, 1990; *Chuang and Wu*, 1991; *Hu and Chang*, 1992; *Tang and Yang*, 1993]. Some authors [e.g., *Hu and Chang*, 1992] attribute the variability to local phenomena such as monsoon, whereas some [e.g., *Tang and Yang*, 1993] believe that the variability is triggered by a remote phenomenon such as the change in the behavior of the North Equatorial Current. Abundant studies on the time-varying Kuroshio south

Table 3. Estimated Parameters Associated With the Kuroshio Current in Four Seasons and One Year

Track	Longitude[a]	Latitude[a]	Maximum Velocity, cm s^{-1}	Height Jump, cm	Along-Track Width, km
			Fall		
d004	138.521	33.053	49	46±14	109±32
d017	131.333	30.656	27	24±08	112±39
d030	124.790	26.764	86	90±22	147±36
d055	133.221	32.397	41	14±09	40±26
d068	126.737	28.573	103	109±20	141±26
d081	121.458	21.632	76	41±17	93±38
d093	135.820	32.819	88	100±22	133±30
d106	129.042	29.615	92	74±13	103±18
d119	122.968	24.611	48	24±09	77±30
			Winter		
d004	138.332	33.379	61	42±10	79±18
d017	131.504	30.322	80	41±05	65±08
d030	124.765	26.809	82	88±23	151±39
d055	133.297	32.254	37	17±08	53±24
d068	126.877	28.285	105	176±53	225±68
d081	121.434	21.678	79	45±19	97±41
d093	135.869	32.723	102	102±16	118±19
d106	129.038	29.614	123	96±12	100±13
d119	122.677	25.232	36	15±08	61±32
			Spring		
d004	138.990	32.206	60	100±40	198±79
d017	131.429	30.463	65	31±06	59±11
d030	124.762	26.810	78	89±25	160±46
d055	133.216	32.393	50	40±10	96±23
d068	126.706	28.618	97	109±23	149±31
d081	121.348	21.871	103	80±24	134±40
d093	135.839	32.769	102	124±22	142±25
d106	129.034	29.613	100	73±11	94±15
d119	122.449	25.712	37	19±09	77±37
			Summer		
d004	138.649	32.818	104	99±14	111±16
d017	131.502	30.324	48	27±05	71±14
d030	124.787	26.763	78	105±36	190±66
d055	133.217	32.395	60	8±07	17±15
d068	126.732	28.572	101	110±21	145±28
d081	121.474	21.582	69	17±07	43±18
d093	135.815	32.818	116	140±25	142±25
d106	129.061	29.567	121	92±12	98±13
d119	122.961	24.610	89	66±14	112±24
			Year		
d004	138.545	33.005	46	43±14	109±35
d017	131.504	30.323	54	30±05	69±12
d030	124.788	26.763	82	95±27	164±46
d055	133.218	32.395	46	6±07	14±19
d068	126.733	28.571	100	118±25	157±33
d081	121.413	21.727	91	63±17	120±32
d093	135.843	32.770	101	113±19	132±23
d106	129.038	29.614	107	82±12	98±14
d119	122.786	24.994	35	22±05	95±20

[a]Longitude and latitude specify the location of maximum velocity.

of Japan are also available [e.g., *Taft*, 1972; *Mizuno and White*, 1983]. In particular, *Mizuno and White* [1983] attribute most of the variability south of Japan to a standing wave and a propagating wave in the Kuroshio System.

Large Scale Circulation Over the Western Pacific and Its Impact on the Kuroshio

The Kuroshio Current is initiated by the North Equatorial Current [*Hu and Chang*, 1992] which is the equa-

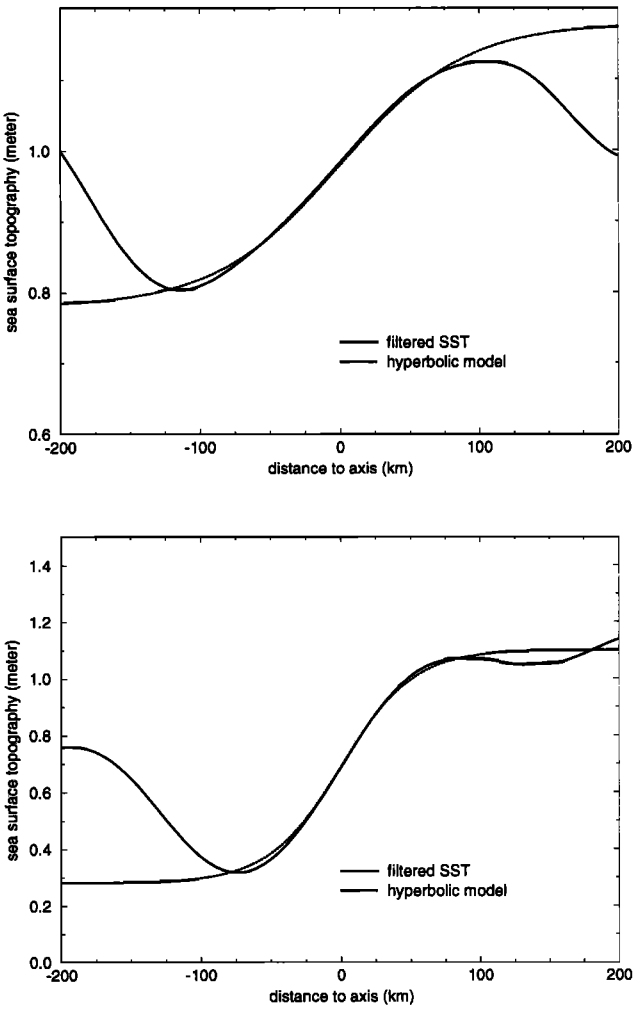

Figure 8. Comparisons between the filtered SST and the hyperbolic models for (top) track d119 and (bottom) track d017. The SST values are from the 1-year data. The zero distance corresponds to the point of maximum velocity, and the distance is negative before this point.

torward arm of the subtropical gyre that spans the entire Pacific Ocean [*Apel*, 1987]. The subtropical gyre is clearly visible in a low degree spherical harmonic expansion of the T/P SST; see, e.g., *Tapley et al.* (1994b) and *Nerem et al.* [1994]. Our area of study covers only a small portion of the oceans; thus a new technique other than the spherical harmonic expansion is needed to identify the gyre. We use the median filter [*Naess and Bruland*, 1989] to do this. The median filter performs the best comparing to other filters such as the Gaussian filter, the boxcar filter (simple average), and the cosine filter. By "best" we mean the resulting SST agrees best with historical data in the overall structure of Pacific's circulation system. The next question is how to determine the filter width. A filter width corresponds to the maximum degree in a spherical harmonic expansion. Thus, e.g., filter widths of 2001, 1334, 1000, 834, and 556 km correspond to maximum degrees of 10, 15, 20, 24, and 36, respectively. Figure 13 shows the SST and the patterns of the geostrophic flows over the Western Pacific in four seasons using a filter width of 1334 km. Figure 13 depicts circulation systems similar to the results by other researchers working on the T/P SST, e.g., *Tapley et al.* [1994b], *Nerem et al.* [1994], and *Knudsen* [1994]. The most pronounced difference in the four SST maps is the structure of the streamlines east and north of Taiwan. Also, a distinct high over the Philippine Sea is found in summer, fall, and winter. This high is also found by *Tapley et al.* [1994b, Plate 5] and may be closely related to the annual cycle detected by *Knudsen* [1994, Plate 1]. The high is believed to be caused by the annual heating [*Tapley et al.*, 1994b].

Now turning to the South China Sea, one sees from Figure 13 very distinct structures of SST in the four seasons. In the summer the sea surface rises by about 10 cm with respect to the sea level of winter. In the spring a warm ring with a radius of about 300-400 km and the center at about 15°N, 113°E is clearly visible and in the summer it becomes somewhat degenerated, but in the fall and winter it shows no sign of existence. At this 1334-km spatial scale the flows in the South China Sea are consistently clockwise. The rise of the sea level in spring and summer is probably due to heating, but not the spill of the water from the Pacific, because in these two seasons the flow vectors at Bashi Channel are pointing toward the Pacific Ocean. On the other hand, in the fall and winter the Kuroshio enters the South China Sea at about 20°N via the Bashi Channel when the gyre's energy is the lowest.

Previously, we mentioned the possible causes of the Kuroshio's variability northeast of Taiwan. We will now see the link between the variability and the kinetic energy of the subtropical gyre at the Western Pacific. The mean kinetic engergy per unit mass at a geographical location (ϕ, λ) is defined as [*Garraffo et al.*, 1992]

$$K_m = \frac{1}{2} v^2(\phi, \lambda) \tag{23}$$

where v is the geostrophic velocity. Assuming a constant thickness for the layer of the geostrophic flow and a constant water density, the spatially averaged mean kinetic energy per unit mass over the studied area is

$$\bar{K}_m = \frac{1}{2}\frac{1}{A}\int_A v^2(\phi, \lambda)\, dA \tag{24}$$

where A is the area. The square root of $\bar{K}_m$ is proportional to the rms velocity of the geostrophic flow:

$$\text{rms} \quad \text{velocity} = \sqrt{\frac{1}{A}\int_A v^2(\phi, \lambda)\, dA} \tag{25}$$

which may be used as a descriptor for the dynamics of the geostrophic flow. Using a filter length of 1334 km for the SST and a numerical integration over the Western Pacific, we obtained with (25) rms velocities of 34.8, 38.4, 34.4, and 34.8 cm s^{-1} for the spring, summer, winter, and fall, respectively. Since the width of the Kuroshio front is of the order of 100 km, the calculated rms velocities according to (25) with the 1334-km fil-

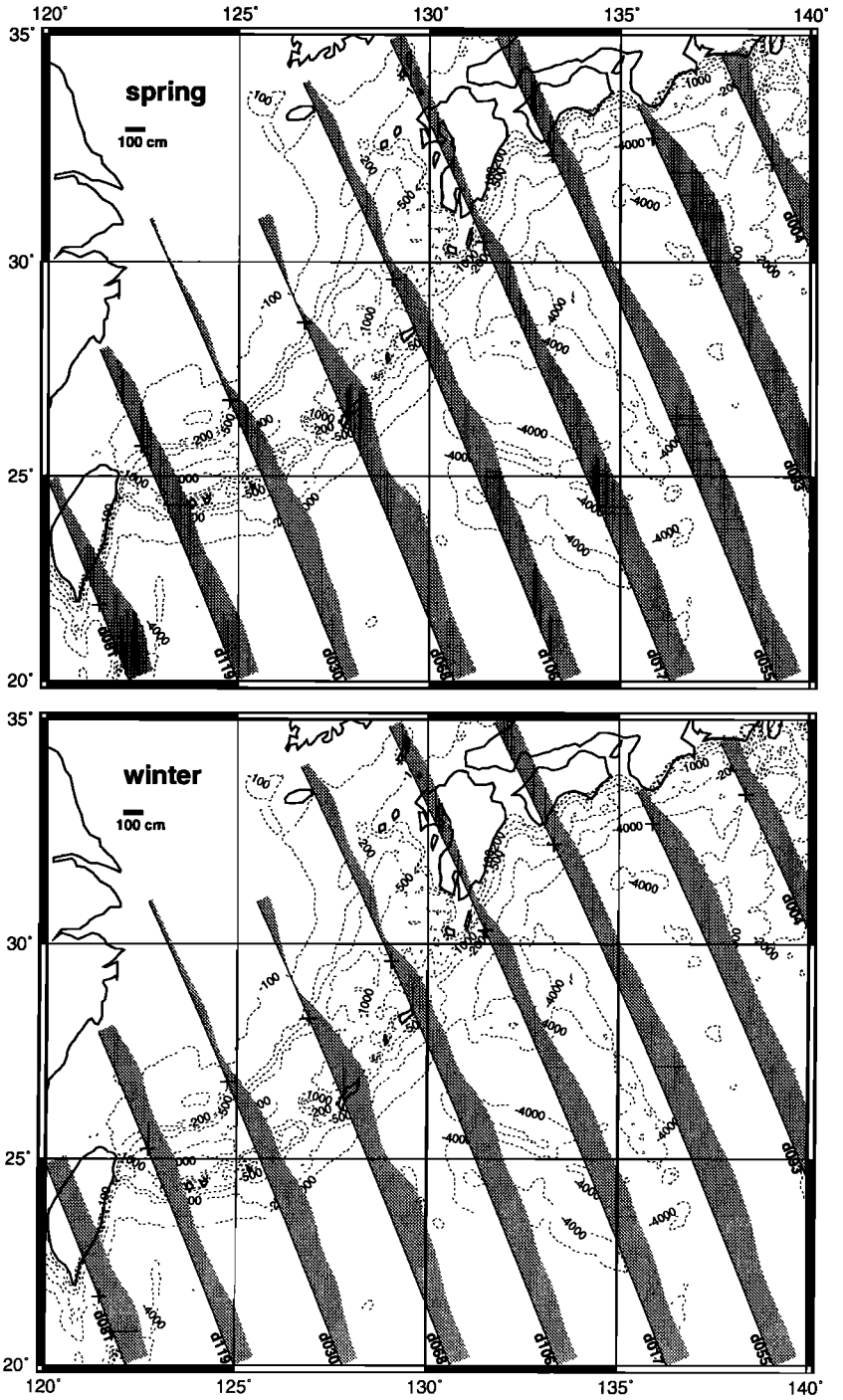

Figure 9. The filtered along-track SST in four seasons. The Gaussian filter with a width of 50 km is used. The crosses mark the locations of the maximum velocities, corresponding to the axes of the Kuroshio. The 100-cm bar shows the scale of SST measured perpendicular from the ground track.

tered SST are independent of the front of the Kuroshio along each of the T/P ground tracks. Figure 14 compares the gyre's rms velocities and the Kuroshio's maximum velocities, height jumps, along-track width, and distances of the axis to the mean axis northeast of Taiwan, which are taken from Table 3 at track d119. Figure 14 shows that although the data used are very sparse, the gyre's rms velocities may be correlated with the first three parameters. This means that the Kuroshio's variability northeast of Taiwan may be triggered by the change of the gyre's kinetic engergy. When the gyre gains its maximum kinetic energy in the summer by perhaps heating, the Kuroshio's velocity, height jump (equivalently the baroclinic transport), and width be-

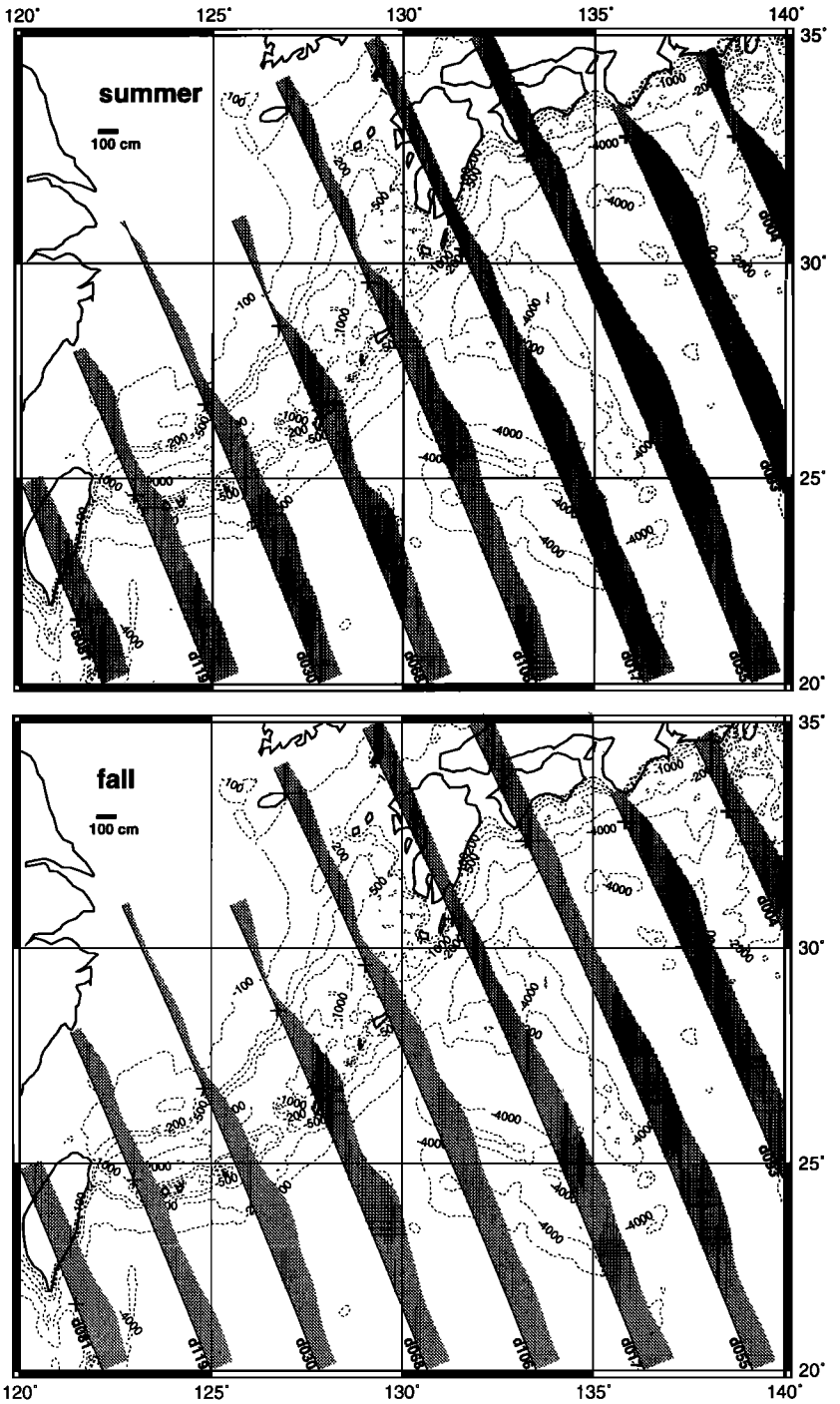

Figure 9. (continued)

come the largest among the four seasons. These quantities start to decline in the fall and reach the minimum in the winter when the gyre's kinetic energy is at its low.

Discussion and Conclusion

In this study the T/P altimeter system has been verified over the Western Pacific, and an altimetric-gravimetric geoid was constructed which together with the T/P altimeter data was used to identify the Kuroshio fronts and its seasonal fluctuations. This local geoid is better than the geoid from OSU91A to degree 360 in both accuracy and resolution. However, due to the data quality and density the current model has an accuracy of only 5-40 cm and is not the best; in the future we may construct a better geoid with improvements such as using more ERS 1/GM data, 3 years of T/P data, and incorporating more marine and land gravity anomalies from China, Philippine, and Japan.

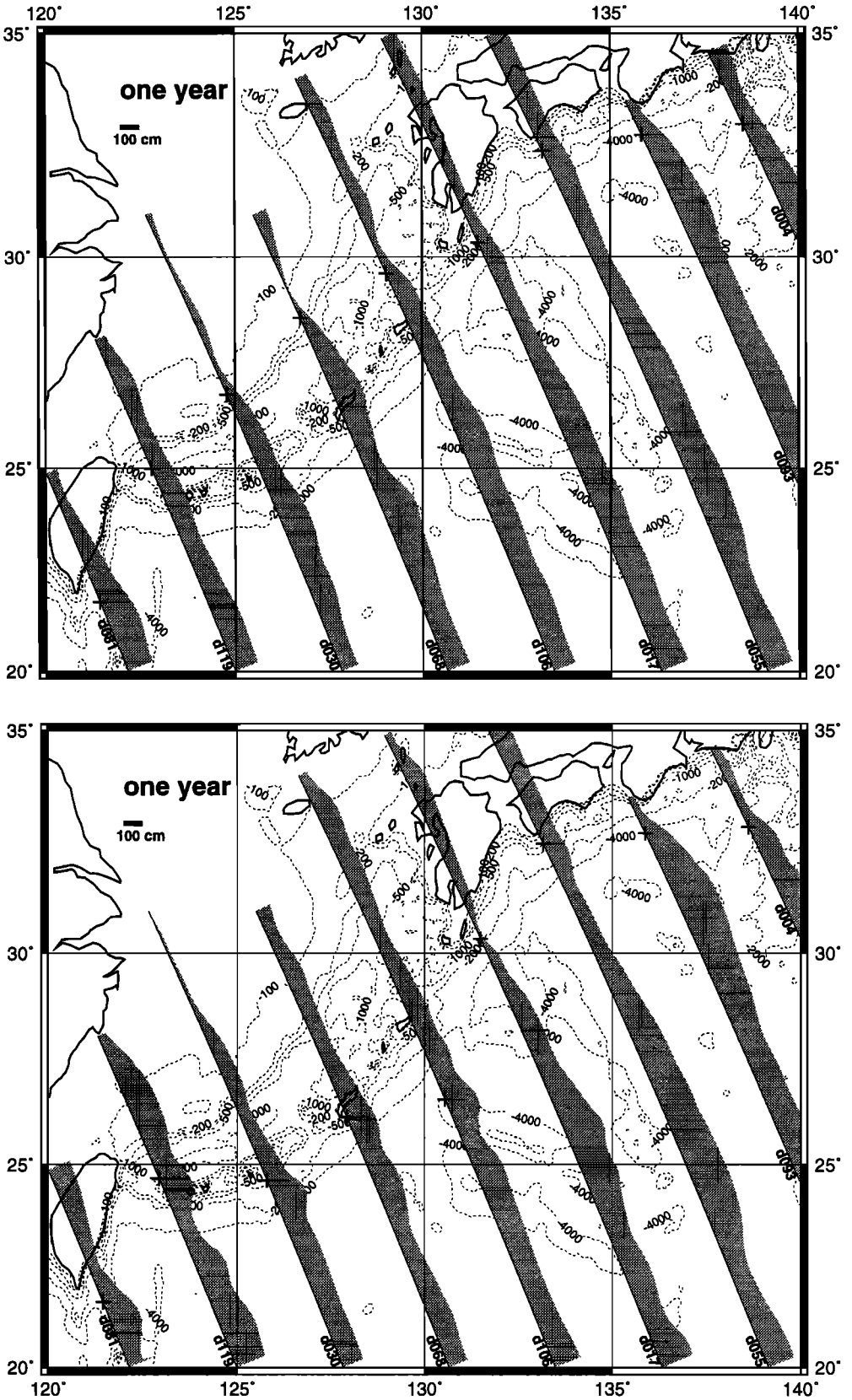

Figure 10. Same as Figure 9, but from 1 year of data. The SST in the upper panel are referenced to the altimetric-gravimetric geoid, and the SST in the lower panel are referenced to the geoid from OSU91A to degree 360.

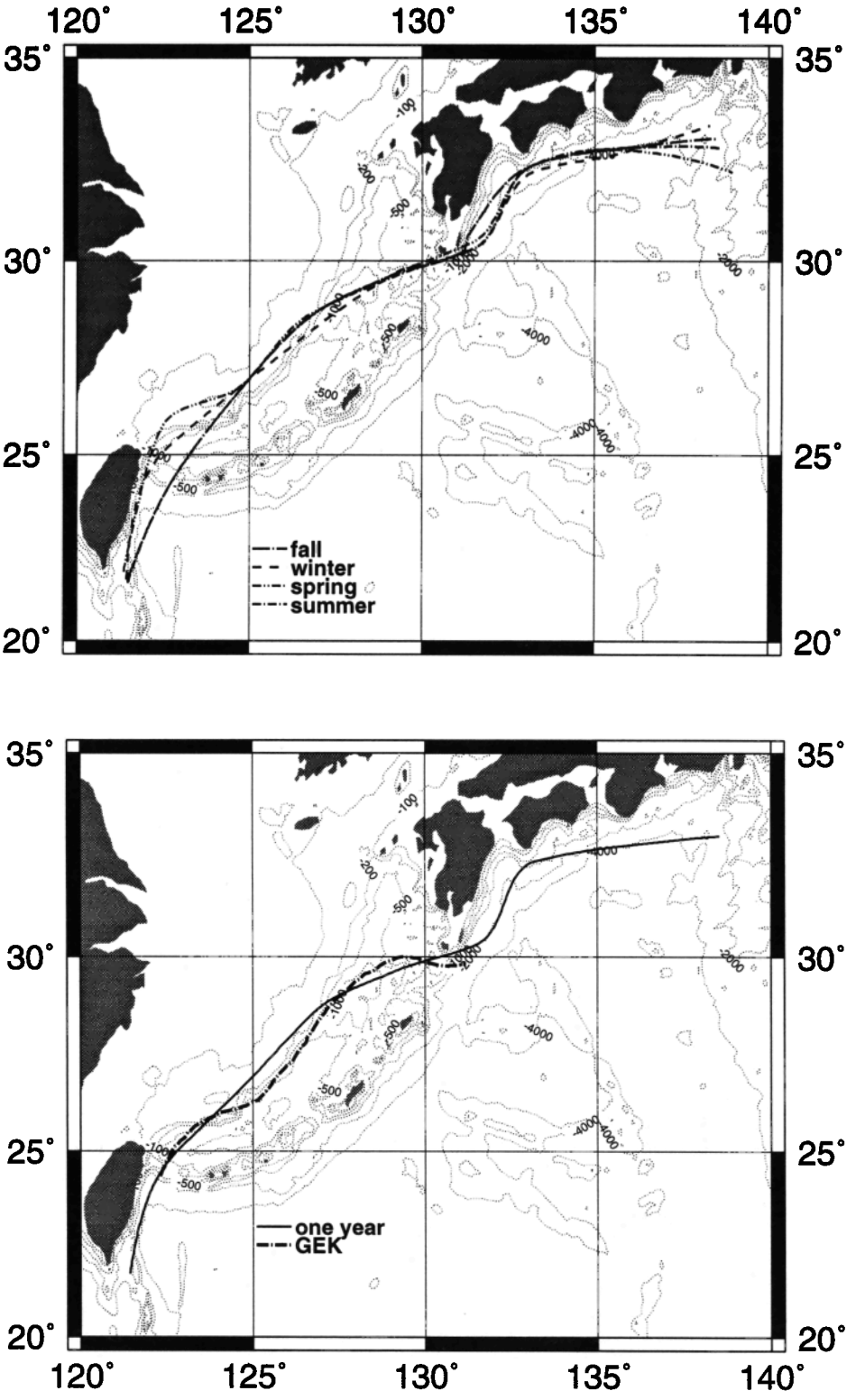

Figure 11. (top) The paths of the Kuroshio in four seasons and (bottom) the mean path for 1 year. Also plotted is the bathymetry (dotted lines) at selected depths. In the lower panel the path based on 32-year Geomagnetic Electro-Kinetograph (GEK) observations is also plotted.

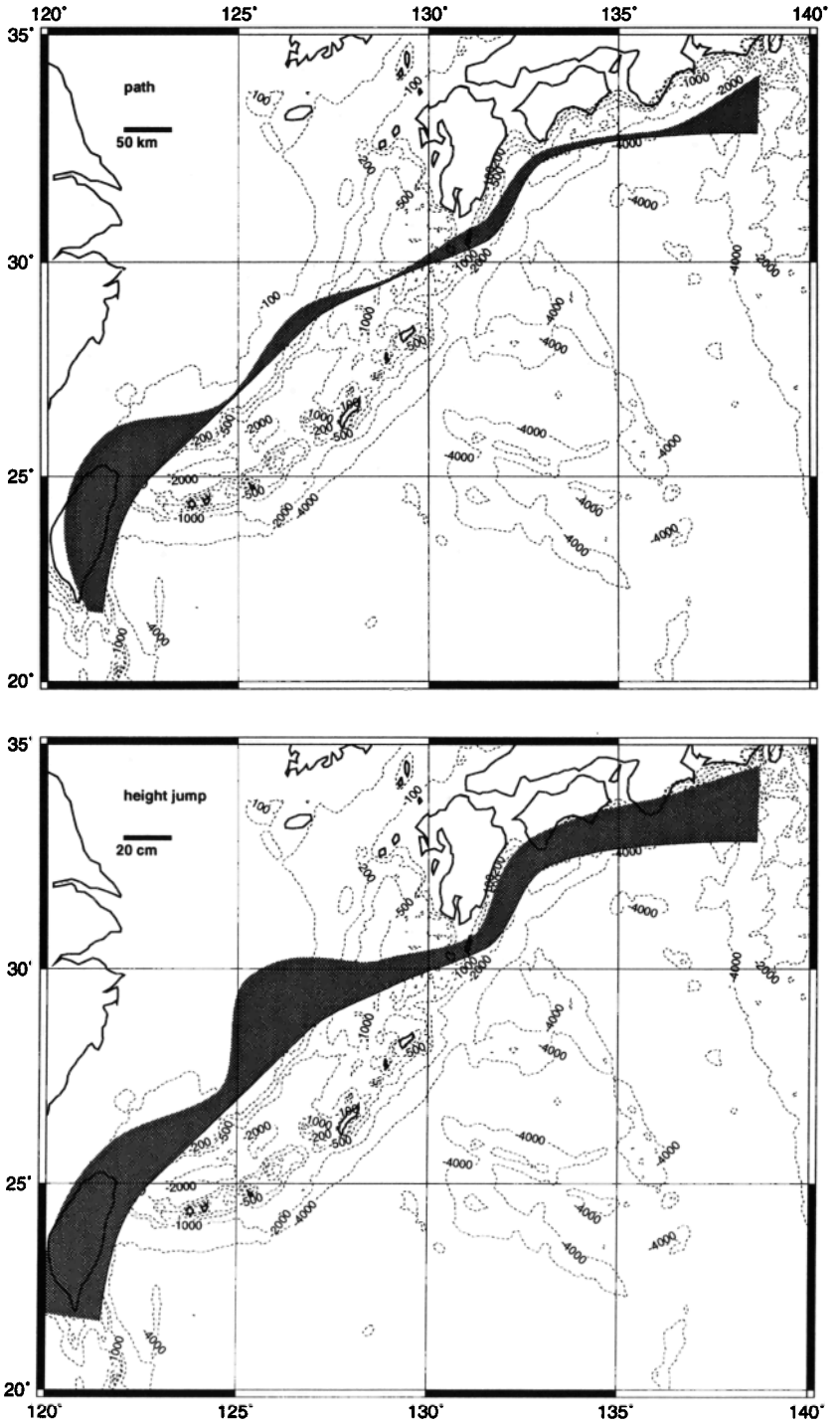

Figure 12. Seasonal variabilities in the Kuroshio's path, maximum velocity, height jump (or baroclinic transport), and along-track width. The variabilities are interpolated using splines and are plotted along the mean path. One-meter height jump corresponds to 50-Sv baroclinic transport.

Also, the covariance models of SST gradient may be refined if a promising global SST model is available. Finally, one can easily extend the geoid modeling and data analysis to the Kuroshio Extension.

With a two-step procedure we have quantified the Kuroshio's seasonal variabilities in the path, maximum velocity, baroclinic transport, and the width of the Kuroshio front. On average the percentage variability of the Kuroshio is about 25% with the largest values found near the northeast coast of Taiwan and the starting point of the Kuroshio Extension. The mean variability of the Kuroshio's path is 22 km, so the Kuroshio probably does not meander as much as the Kuroshio Extension and the Gulf Stream do. Because of the

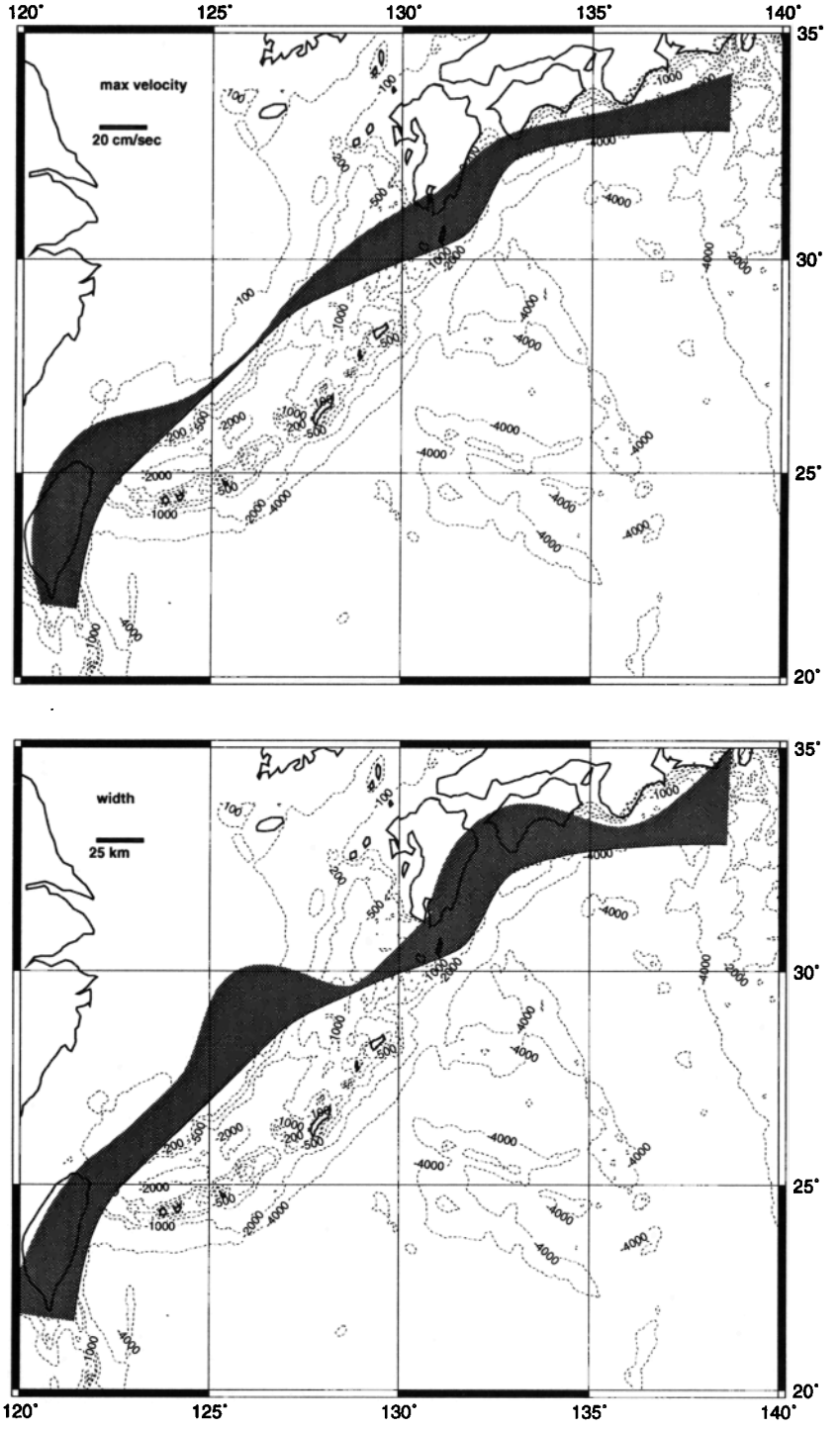

Figure 12. (continued)

low path variability in most part of the Kuroshio we believe that a long-term averaged sea surface over the Kuroshio contains just the signals we are looking for and one should not use it as the level surface for determining the SST; see more discussion by *Rapp and Smith* [1994]. Furthermore, because of the near 300-km cross-track spacing of T/P the resolutions of our results on various aspects are low. For example, we cannot account for the sharp turn of the Kuroshio at about 30°N, 129°E. The resolutions may be improved by using the ERS 1 35-day data concurrent with the T/P data between October 1992 and December 1993. However, we must first correct ERS 1's orbit before doing so, or one may try the newly adjusted ERS 1 data from *Traon et al.* [1995] which were reported to have the same orbital accuracy as T/P. The best geometry will be obtained if we have a constellation of altimeter satellites. This is not impossible considering the ongoing missions such as T/P,

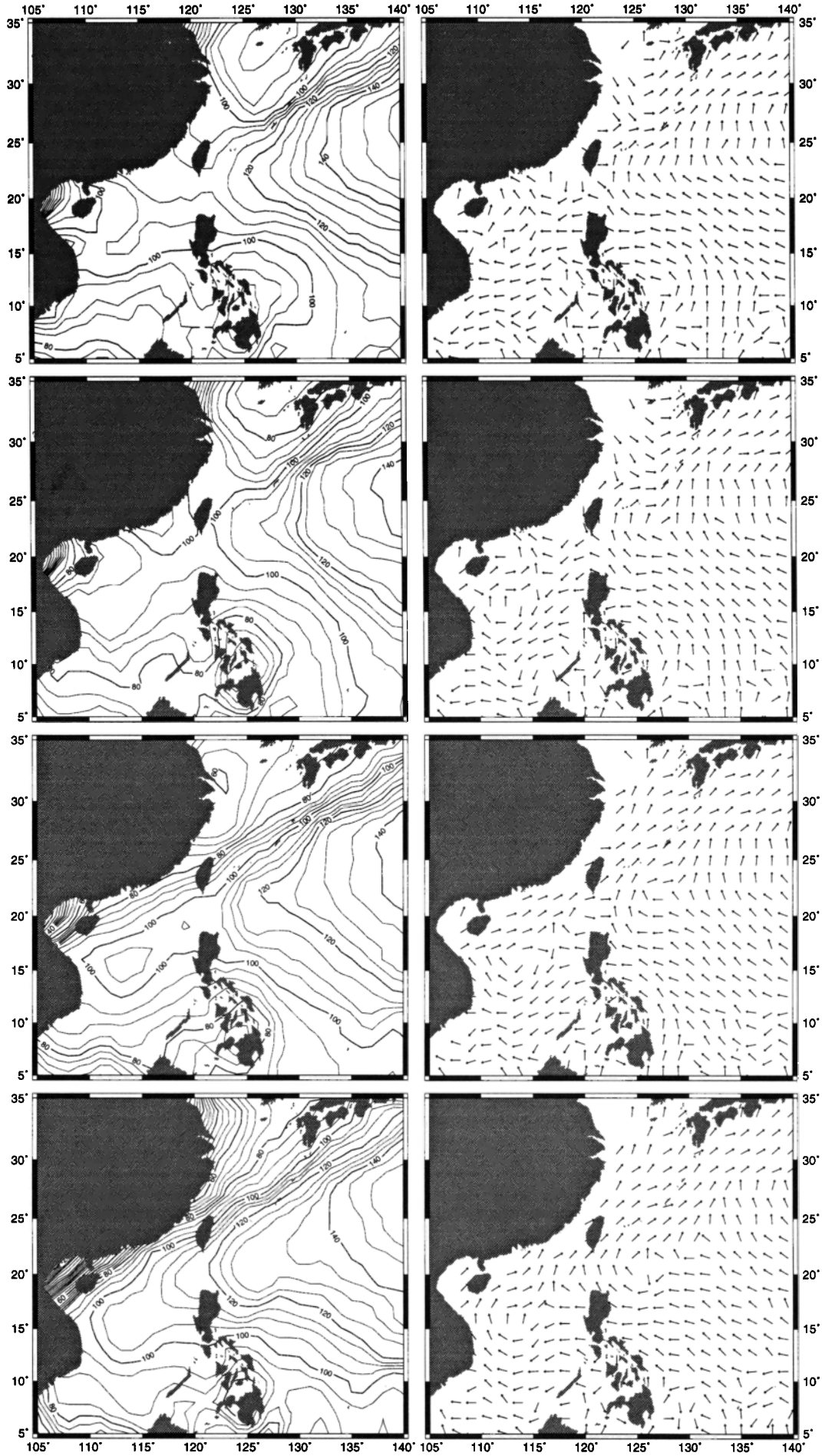
105° 110° 115° 120° 125° 130° 135° 140°
35° 30° 25° 20° 15° 10° 5°

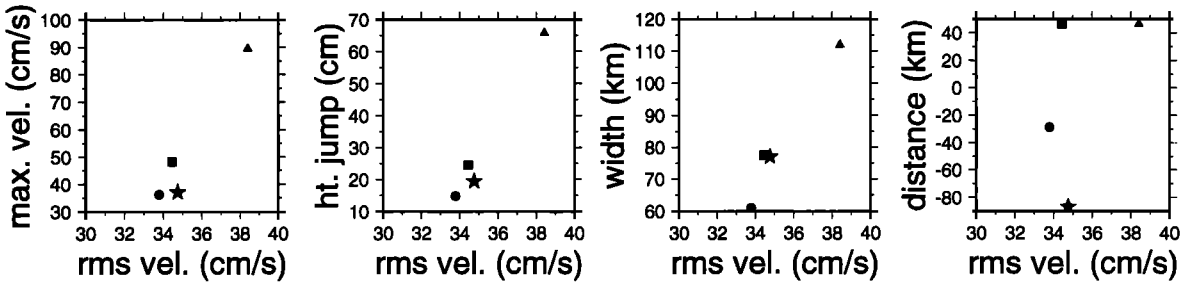

Figure 14. The relationships between the low-frequency kinetic energy of the Western Pacific circulation, represented by its rms velocity, and the Kuroshio's maximum velocity, height jump, along-track width, and distance of the axis to the mean axis near the northeast coast of Taiwan (from left to right). The distance to the left of the mean axis is negative and to the right is positive. The symbols used are star, spring; triangle, summer; square, fall; circle, winter.

ERS 1, ERS 2, and other planned altimeter missions (see Table 9.2 of *Seeber* [1993]). Furthermore, in theory one can study the high-frequency variability of the Kuroshio on a 10-day basis as given by *Rapp and Smith* [1994], but we wish to wait for the new generation of T/P GDR which contains improved geophysical corrections (especially the ocean tide correction) and should give more promising results than the current T/P data.

Appendix A: Derivatives of Legendre's Polynomials When t = ±1

When $t = \pm 1$ in (10) and (11), we must evaluate the two series in a different way. From *Lebedev* [1972], we have the formula for calculating the first derivative of Legendre's polynomial:

$$P_n'(t) = \frac{n}{1-t^2}P_{n-1}(t) - \frac{nt}{1-t^2}P_n(t) \qquad \text{(A1)}$$

If $t = 1$, by applying L'Hospital's rule, we get

$$\begin{aligned} P_n'(1) &= n \lim_{t\to 1} \frac{P_{n-1}(t) - tP_n(t)}{1-t^2} \\ &= n \lim_{t\to 1} \frac{P_{n-1}' - P_n - tP_n'}{-2t} \\ &= \frac{-n}{2}\left[P_{n-1}'(1) - P_n(1) - P_n'(1)\right] \qquad \text{(A2)} \end{aligned}$$

Since $P_n(1) = 1$, we get the recursive formula for $P_n'(1)$:

$$P_n'(1) = \frac{n}{n-2}P_{n-1}'(1) - \frac{n}{n-2}, \quad n > 2 \qquad \text{(A3)}$$

with the starting values $P_0'(1) = 0, P_1'(1) = 1$, and $P_2'(1) = 3$.

Similarly, if $t = -1$ (it is almost impossible to encounter this case), then we have the recursive formula for $P_n'(-1)$:

$$P_n'(-1) = \frac{n}{2-n}P_{n-1}'(-1) - \frac{n(-1)^n}{2-n}, \quad n > 2 \qquad \text{(A4)}$$

with the starting values $P_0'(-1) = 0, P_1'(-1) = 1$, and $P_2'(-1) = -3$.

Using the above procedure, one may also derive a recursive formula for $P_n''(1)$. However, this special case corresponds to computing $C_{ll}^{\zeta}(0)$, which is equal to $C_{mm}^{\zeta}(0)$, so such a formula is not needed in this study. Also, the formula for $P_n''(-1)$ is not needed since this case is unlikely to happen.

Appendix B: Prediction Formulae for LSC and the Scaling Factors

The global covariance functions must be scaled to reflect the true variance of the data used in a inversion cell (plus data border). In the context of this study, two scaling factors must be found. The first one is for both the covariance functions of geoid gradient and gravity anomaly and is calculated as the weighted mean of the scaling factors for geoid gradient and gravity anomaly:

$$\alpha_T = \frac{n\alpha_1 + m\alpha_2}{n+m} \qquad \text{(B1)}$$

where n and m are the numbers of geoid gradients and gravity anomalies, respectively, in an inversion cell (plus data border). The value α_1 is computed as

$$\alpha_1 = \frac{\bar{\sigma}_\epsilon^2}{C_{ll}^{\epsilon}(0)} \qquad \text{(B2)}$$

where $\bar{\sigma}_\epsilon^2$ is the variance of the geoid gradients and $C_{ll}^{\epsilon}(0)$ is the variance of the global covariance function of geoid gradient. Similarly, the value α_2 is is computed as

$$\alpha_2 = \frac{\bar{\sigma}_{\Delta g}^2}{C_{\Delta g}(0)} \qquad \text{(B3)}$$

where $\bar{\sigma}_{\Delta g}^2$ is the variance of the gravity anomalies and $C_{\Delta g}(0)$ is the variance of the global covariance function of gravity anomaly.

Figure 13. Filtered SST (in centimeters) and corresponding circulation patterns in four seasons (from top to bottom are fall, winter, spring, and summer). The median filter with a width of 1334 km is used.

The second scaling factor is for the global covariance function of SST gradient and is computed as

$$\alpha_\theta = \frac{\zeta_x^2 + \zeta_y^2}{C_{ll}^{\zeta}(0)} \tag{B4}$$

where ζ_x and ζ_y are the gradients of the *Levitus* [1982] SST along the longitudinal and latitudinal directions, respectively. The position to compute ζ_x and ζ_y is located at the center of an inversion cell. In reality we constructed a global grid of α_θ at a 1° × 1° interval, and the needed value is interpolated from this grid in a LSC computation.

With the scaling factors α_T and α_θ, a predicted geoidal height is then

$$N = N_{ref} + [\alpha_T \mathbf{C_{N\epsilon}}\ \alpha_T \mathbf{C_{N\Delta g}}] \cdot \begin{bmatrix} \alpha_T \mathbf{C_\epsilon} + \alpha_\theta \mathbf{C_\theta} + \mathbf{D_e} & \alpha_T \mathbf{C_{\epsilon\Delta g}} \\ \alpha_T \mathbf{C_{\Delta g\epsilon}} & \alpha_T \mathbf{C_{\Delta g}} + \mathbf{D_{\Delta g}} \end{bmatrix}^{-1} \begin{bmatrix} \mathbf{e} \\ \mathbf{\Delta g} \end{bmatrix}$$

$$= N_{ref} + [\mathbf{C_{N\epsilon}}\ \mathbf{C_{N\Delta g}}] \cdot \begin{bmatrix} \mathbf{C_\epsilon} + \frac{1}{\alpha_T}(\alpha_\theta \mathbf{C_\theta} + \mathbf{D_e}) & \mathbf{C}_{\epsilon\Delta g} \\ \mathbf{C_{\Delta g\epsilon}} & \mathbf{C_{\Delta g}} + \frac{1}{\alpha_T}\mathbf{D_{\Delta g}} \end{bmatrix}^{-1} \cdot \begin{bmatrix} \mathbf{e} \\ \mathbf{\Delta g} \end{bmatrix} \tag{B5}$$

and the error variance of N is

$$\sigma_N^2 = \alpha_T \{C_N(0) - \begin{bmatrix} \mathbf{C_{N\epsilon}} & \mathbf{C_{N\Delta g}} \end{bmatrix} \cdot \begin{bmatrix} \mathbf{C_\epsilon} + \frac{1}{\alpha_T}(\alpha_\theta \mathbf{C_\theta} + \mathbf{D_e}) & \mathbf{C_{\epsilon\Delta g}} \\ \mathbf{C_{\Delta g\epsilon}} & \mathbf{C_{\Delta g}} + \frac{1}{\alpha_T}\mathbf{D_{\Delta g}} \end{bmatrix}^{-1} \cdot \begin{bmatrix} \mathbf{C_{\epsilon N}} \\ \mathbf{C_{\Delta gN}} \end{bmatrix}\} \tag{B6}$$

In the above two equations, the definitions are

N_{ref} reference geoidal height;

$C_N(0)$ variance of the global covariance function of geoid;

e vector containing SSG;

$\mathbf{\Delta g}$ vector containing gravity anomalies;

$\mathbf{D_e}$ diagonal matrix containing the error variances of SSG;

$\mathbf{D_{\Delta g}}$ diagonal matrix containing the error variances of gravity anomalies; we used an uniform value of 1 mgal^2 in this study;

$\mathbf{C_{N_\epsilon}}$ covariance matrix between geoid and geoid gradient; $\mathbf{C_{N_\epsilon}} = \mathbf{C_{\epsilon N}^T}$;

$\mathbf{C_{N\Delta g}}$ covariance matrix between geoid and gravity anomaly; $\mathbf{C_{N\Delta g}} = \mathbf{C_{\Delta gN}^T}$;

$\mathbf{C_\epsilon}$ covariance matrix of geoid gradient;

$\mathbf{C_\theta}$ covariance matrix of SST gradient;

$\mathbf{C_{\epsilon\Delta g}}$ covariance matrix between geoid gradient and gravity anomaly; $\mathbf{C_{\epsilon\Delta g}} = \mathbf{C_{\Delta g\epsilon}^T}$;

$\mathbf{C_{\Delta g}}$ covariance matrix of gravity anomaly.

The LSC computations can be made using the inversion-free scheme described by *Hwang and Parsons* [1995].

Acknowledgments. This work is supported by the National Science Council of the Republic of China, under contract NSC84-2211-E-009-032. Supercomputer resources were kindly provided by the National Center for High Performance Computing via this project. The free software GMT [*Wessel and Smith*, 1991] was used to display most of the data.

References

Apel, J. R., *Principles of Ocean Physics*, Academic, San Diego, Calif., 1987.

Archiving, Validation, and Interpretation of Satellite Data in Oceanography (AVISO), *AVISO User Handbook: Merged TOPEX/POSEIDON Products, Rep. AVI-NT-02-101-CN*, Ed. 2.1, Cent. Natl. d'Etudes Spatiales, Toulous, France, 1992.

Chern C. S., J. Wang, and D. P. Wang, The exchange of Kuroshio and East China Sea shelf water, *J. Geophys. Res., 95*, 16,017-16,023, 1990.

Chuang, W. S., and C. K. Wu, Slope current fluctuations northeast of Taiwan, *J. Oceanogr. Soc. Jpn., 47*, 185-193, 1991.

de Boor, C., *A Practical Guide to Splines*, Springer-Verlag, New York, 1978.

Denker, H., *Radial orbit reduction and sea surface topography determination using one year of Geosat altimeter data, Rep. 404*, Dep. of Geod. Sci. and Surv., Ohio State Univ., Columbus, 1990.

Eanes, R. J., C. K. Shum, X. C. Ma, and B. D. Tapley, Implications of ocean tide model error for altimetric determination of sea surface topography, Eos Trans. AGU, 74(43), Fall Meeting Suppl., 188, 1993.

Engelis, T.,*Spherical harmonic expansion of the Levitus sea surface topography, Rep. 385*, Dep. of Geod. Sci. and Surv., Ohio State Univ., Columbus, 1987.

Escudier, P., N. Picot, and O. Z. Zanife, Altimetric ionospheric correction using DORIS Doppler data, in *Environmental Effects on Spacecraft Positioning and Trajectories, Geophys. Mono. 73*, edited by A. V. Jones, pp. 61-72, AGU, Washington, DC, 1993.

Fu, L. L., E. J. Christensen, C. A. Yamarone Jr., M. Lefebvre, Y. Ménard, M. Dorrer, and P. Escudier, TOPEX/POSEIDON mission overview, *J. Geophys. Res., 99*, 24,369-24,381, 1994.

Garraffo, A., S. G. Garzoli, W. Haxby, and D. Olson, Analysis of a general circulation model, 2, Distribution of the kinetic energy in the South Atlantic and Kuroshio/Oyashio Systems, *J. Geophys. Res., 97*, 20,139-20,153, 1992.

Hu, J. H., and J. L Chang, The variability of hydrographic fields at the Kuroshio's turning on northeast of Taiwan, *Terr. Atmos. Oceanic Sci. (TAO), 3*, 277-292, 1992.

Hwang, C., and B. Parsons, Gravity anomalies derived from Seasat Geosat, ERS-1 and TOPEX/POSEIDON altimetry and ship gravity: A case study over the Reykjanes Ridge, *Geophys. J. Int., 122*, 551-568, 1995.

Imel, D. A., Evaluation of the TOPEX/POSEIDON dual-frequency ionosphere correction, *J. Geophys. Res., 99*, 24,895-24,906, 1994.

Knudsen, P., Global low harmonic degree models for the seasonal variability and residual ocean tides from TOPEX/POSEIDON altimeter data, *J. Geophys. Res., 99,* 24,619-24,632, 1994.

Lebedev, N. N., *Special Functions and Their Applications,* translated from Russian by R. A. Silverman, Dover, Mineola, N. Y., 1972.

Levitus, S., *Climatological Atlas of the world ocean, NOAA Prof. Pap. 13,* 1982.

Ma, X. C., C. K. Shum, R. J. Eanes, and B. D. Tapley, Determination of ocean tides from the first year of TOPEX/POSEIDON altimeter measurements, *J. Geophys. Res., 99* , 24,809-24,820, 1994.

Marsh, J. G., and E. S. Chang , 5′ detailed gravimetric geoid in the northern Atlantic Ocean, *Mar. Geod., 1,* 359-378, 1978.

Mazzega, P., and M. Bergé, Ocean tides in the Asia semi-closed seas from TOPEX/POSEIDON, *J. Geophys. Res., 99,* 24,867-24,882, 1994.

Mizuno, K., and W. B. White, Annual and interannual variability in the Kuroshio Current System, *J. Phys. Oceanogr., 13,* 1847-1867, 1983.

Moritz, H., *Advanced least-squares methods, Rep. 175,* Dep. of Geod. Sci. and Surv., Ohio State Univ., Columbus, 1972.

Moritz, H., *Advanced Physical Geodesy,* Abacus, Karlsruhe, 1980.

Naess, O. E., and L. Bruland, Improvement of the multichannel seismic data through the application of the median concept, *Geophys. Prospect., 37,* 225-241, 1989.

Nerem, R. S., E. J. Schrama, C. J. Koblinsky, and B. D. Beckley, A preliminary evaluation of ocean topography from the TOPEX/POSEIDON mission, *J. Geophys. Res., 99,* 24,565-24,583, 1994.

Pickard, G. L., and W. J. Emery, *Descriptive Physical Oceanography, An Introduction,* 4th ed., Pergamon, Tarrytown, N. Y., 1982.

Porter, D. L., E. Dobson, and S. Glenn, Measurements of sea surface topography during SYNOP utilizing a Geosat synthetic geoid, *Geophys. Res. Lett., 19,* 1847-1850, 1992.

Qiu, B., T. Toda, and N. Imasato, On Kuroshio front fluctuations in the East China Sea using satellite and in situ observational data, *J. Geophys. Res., 95,* 18,191-18,204, 1990.

Rapp, R. H., *Geometric Geodesy, Part I and II,* Dep. of Geod. Sci. and Surv., Ohio State Univ., Columbus, 1989.

Rapp, R. H., Geoid undulation accuracy, *IEEE Trans. Geosci. and Remote Sens., 31,* 365-370, 1993.

Rapp, R. H., and D. A. Smith, Preliminary estimates of the Gulf Stream characteristics from TOPEX data and a precise gravimetric geoid, *J. Geophys. Res., 99,* 24,707-24,724, 1994.

Rapp, R. H., and Y. M. Wang, Dynamic topography estimates using Geosat data and a gravimetric geoid in the Gulf region, *Geophys. J. Int., 117,* 511-528, 1994.

Rapp, R. H., Y. M. Wang, and N. Pavlis, *The Ohio State 1991 geopotential and sea surface topography harmonic coefficient models, Rep. 410,* Dep. of Geod. Sci. and Surv., Ohio State Univ., Columbus, 1991.

Schrama, E. J. O., and R. D. Ray, A preliminary tidal analysis of TOPEX/POSEIDON altimetry, *J. Geophys. Res., 99,* 24,799-24,808, 1994.

Schwarz, K. P., M. G. Sideris, and R. Forsberg, The use of FFT techniques in physical geodesy, *Geophys. J. Int., 100,* 485-514, 1990.

Seeber, G., *Satellite Geodesy: Foundations, Methods and Applications,* Walter de Gruyter, New York, 1993.

Segawa, J., Application of precise altimetry to the study of precise leveling of the sea surface, the Earth's gravity field, and the rotation of the Earth, in *TOPEX/POSEIDON Science Investigations Plan,* pp. 126-130, JPL, Calif., 1991.

Taft, B. A., Characteristics of the flow of the Kuroshio south of Japan, in *Kuroshio, Its Physical Aspects,* edited by S. Stommel and K. Yoshida, pp. 165-216, Univ. of Tokyo Press, Tokyo, 1972.

Tai, C. K., Estimating the surface transport of meandering oceanic jet streams from satellite altimetry: Surface transport estimates for the Gulf Stream and the Kuroshio Extension, *J. Phys. Oceanogr., 20,* 860-879, 1990.

Tai, C. K., and J. M. Kuhn, *On reducing the large-scale time dependent errors in satellite altimetry while preserving the ocean signal: Orbit and tide error reduction for TOPEX/POSEIDON, NOAA Tech. Memo. NOS OES 009,* 1994.

Tang, T. Y., and Y. J. Yang, Low frequency current variability on the shelf break northeast of Taiwan, *J. Oceanogr., 49,* 193-210, 1993.

Tapley, B. D., et al., Precision orbit determination for TOPEX/POSEIDON, *J. Geophys. Res., 99,* 24,383-24,404, 1994a.

Tapley, B. D., D. P. Chambers, C. K. Shum, R. J. Eanes, and J. C. Ries, Accuracy assessment of the large-scale dynamic topography from TOPEX/POSEIDON altimetry, *J. Geophys. Res., 99,* 24,605-24,617, 1994b.

Traon, P. Y., P. Gaspar, F. Bouyssel, and H. Makhmara, Using TOPEX/POSEIDON data to enhance ERS-1 orbit, *J. Atmos. Oceanic Technol., 12,* 161-170, 1995.

Tscherning, C. C., and R. H. Rapp, *Closed expressions for gravity anomalies, geoid undulations and deflections of the vertical implied by anomaly degree variance models, Rep. 208,* Dep. of Geod. Sci. and Surv., Ohio State Univ., Columbus, 1974.

Uotila, U. A., *Notes on adjustment computations,* Part I, Dep. of Geod. Sci. and Surv., Ohio State Univ., Columbus, 1986.

Wessel, P., and W. H. Smith, Free software helps map and display data, *Eos Trans. AGU, 72(41),* 441, 445-446, 1991.

Wessel, P., and A. B. Watts, On the accuracy of the marine gravity measurements, *J. Geophys. Res., 93,* 393-413, 1988.

Yen, H. Y., C. H. Lin, G. K. Yu, and Y. B. Tsai, Free-air gravity map of Taiwan and its applications, *Terr. Atmos. Oceanic Sci. (TAO), 1,* 143-155, 1990.

Zlotnicki, V., Sea level differences across the Gulf Stream and Kuroshio Extension, *J. Phys. Oceanogr.*, 21, 599-609, 1991.

Zlotnicki, V., Quantifying time-varying oceanographic signals with altimetry, in *Lecture Notes in Earth Science,* vol. 50, edited by R. Rummel and F. Sansò, pp. 144-189, Springer-Verlag, New York, 1993.

C. Hwang, Department of Civil Engineering, National Chiao Tung University, 1001 Ta Hsuej Road, Hsinchu 30050, Taiwan. (e-mail: hwang@geodesy.cv.nctu.edu.tw)

(Received August 4, 1995; revised December 5, 1995; accepted December 14, 1995.)